NTNU
Norwegian University of
Science and Technology

Scalar wave scattering from two-dimensional, randomly rough surfaces

Torstein Storflor Hegge

Master of Science in Physics and Mathematics
Submission date: June 2011
Supervisor: Ingve Simonsen, IFY

Norwegian University of Science and Technology
Department of Physics

Abstract

We study scalar waves scattered from self-affine and Gaussian correlated surfaces. The simulations are performed using rigorous simulation of the integral equations derived from the Helmholtz equation, describing a scalar wave above a non-penetrable surface with a hard wall or free surface boundary condition. An incident, Gaussian shaped beam is scattered from the surface, and the full angular distribution of the scattered intensity is obtained. Self-affine and Gaussian correlated random surfaces are generated, and the resulting scattered intensity is averaged over a large number of surfaces (in the order $N_s = 3000$), using the ergodicity of the surface. Compared with analytical calculation of the scattered intensity in the Kirchhoff approximation, our approach gives similar results for less rough surfaces. Compared with simulations of electromagnetic waves scattered from a perfect conductor, without recording the polarisation of the scattered light, our simulations give similar results when using a hard wall boundary condition. We observe phenomena such as specular scattering for less rough surfaces, diffuse forward scattering for more rough surfaces and enhanced backscattering for surfaces where waves scattered multiple times by the surface roughness gives a large contribution to the scattered intensity.

Preface

This master's thesis is the conclusion of a five-year integrated master's programme in applied physics and mathematics at NTNU, Trondheim. The work was carried out at the Department of Physics at NTNU.

I wish to thank my supervisor Ingve Simonsen for good support and valuable feedback while working on this project.

Trondheim, June 27, 2011

Torstein Storflor Hegge

Contents

1 Introduction

We want to determine the scalar wave scattering pattern when an incident beam is scattered from a randomly rough surface, where the surface is described by a hard wall or free surface boundary condition. We consider a large, plane surface with known surface statistics, either with a Gaussian correlation function or a self-affine structure. We want to find a physically measurable size for the scattered intensity in all directions. Obtaining the full angular distribution makes it possible to check the energy conservation. Knowing the scattering pattern gives the possibility to study scattering phenomena such as enhanced backscattering caused by multiple scattering.

A large number of approaches have been used to simulate wave scattering in various applications. Scattering from surfaces can be split into scattering from plane surfaces with a surface structure or from a system with a complex structure. Surfaces found in nature can often be described as correlated, random surfaces where a correlation function describes how the different heights along the surface are located relative to one another. Self-affine surfaces can be found in fractured surfaces, geological structures, metallurgy and biological systems, among others. They remain invariant under a set of transformations over an interval, described a roughness exponent, or Hurst exponent.

Acoustic waves can be described by the linear wave equation, and the Helmholtz equation gives a frequency domain description of the scalar wave. Scalar waves can also be seen as an approximation to electromagnetic, polarized waves. The simplest choice of media is a single surface between a medium allowing wave propagation and a impenetrable medium. The boundary condition for the surface between the media can be described as a hard wall or a free surface.

Our approach is based on rigorous simulation of electromagnetic waves scattered from two-dimensional surfaces with a Gaussian correlation function [10]. For simple scattering systems, the scattered intensity can be obtained analytically. An analytic solution can be obtained for a plane waves scattering from a self-affine surface [14].

Various approximations have been used to obtain approximate solutions for the scattering problem. In general we seek a numerical solution of the wave equation for a volume containing one or more media [4]. The most direct approach is using the Finite Difference Method (FDM), discretising the wave in time and space though approximations of the differential operators. The Finite Element Method (FEM) instead discretises the medium and time into small blocks within which the wave equation can be solved analytically, and then describes the connectivity between the blocks as a linear system of equations. The direct, discrete methods have great generality, but their applicability is limited by the excessive computational requirements.

Other numerical approaches are more efficient, at the cost of reduced generality. A

simple approach is the Kirchhoff approximation, where only single scattering is taken into account, giving a solution only dependent on the local slope of the surface and the Fresnel coefficients for the media at the interface [16]. Using the Rayleigh equation, and the Reduced Rayleigh equation (RRE) [9], gives an approximation where multiple scattering is considered, but only for upward scattered paths. This is a valid approximation for less rough surfaces, as long as the contribution from multiple scattering is limited. A number of approaches is based on various perturbation theories. Perturbation theory can be improved further by introducing a shadowing function, which takes into account how parts of the surface are less illuminated as the surface ridges cast shadows into the nearby valleys [20].

To take into account multiple scattering from strongly rough surfaces a rigorous simulation of the integral equations governing the scattering process is used. This gives a numerical solution for potentially arbitrary rough surfaces, but at the cost of high computational requirements [10].

The scattering of waves from a one-dimensional surface have been studied thoroughly[9], and much of the same techniques used for one-dimensional surfaces can be applied to two-dimensional systems. The main difference lies in the smaller number of unknowns for an one-dimensional surface, making it possible to simulate larger surfaces, no cross polarization and no anisotropic surface structure.

Application of the scalar wave scattering in acoustical modelling focus on complete simulations of propagation and scattering. The sound velocity profile often gives total reflection without hitting the sea bottom, making the exact process on the sea bottom less relevant. A simple representation of the boundary conditions reduces the complexity of the simulation, but at the cost of ignoring some of the effects in the surface and in the lower medium. As the surface roughness is increased, the effect from including multiple scattering increases, and multiple scattering effects such as enhanced backscattering appears.

We have performed simulations of scalar waves scattered from randomly rough, Gaussian correlated and self-affine surfaces using rigorous simulation for a hard wall and soft wall surface. We have studied scattering from self-affine, isotropic surfaces with varying Hurst exponent, $0 < H < 1$, and topothesy, $10^{-2}\lambda < \ell < 10^{-6}\lambda$. We have also studied correlated surfaces with Gaussian correlation function and height-distribution, for both isotropic and anisotropic surfaces. The generated surfaces has RMS-roughness in the interval $0.1\lambda < \delta < \lambda$ and correlation lengths in the interval $\lambda < a < 3\lambda$ (up to $a_2 = 6\lambda$ for anisotropic surfaces).

Our solution is compared with the analytic solution obtained for a plane wave scattered from a self-affine surface in the Kirchhoff approximation. The scalar wave simulation is also compared with rigorous simulation of electromagnetic waves scattered from a perfect conductor.

In chapter 2 the theory behind the simulations is introduced. Chapter 3 described the methods used in the calculations, and in chapter 4 the results from the simulations are presented and discussed.

2 Theory

The system geometry is first introduced, followed by a description of the characteristics of the randomly rough surfaces. The background for acoustic wave scattering is given, and the wave equation for the scalar wave scattering is finally applied to the two-dimensional, randomly rough surface.

2.1 Scattering geometry

The scattering system consists of a rough surface separating vacuum and a non-penetrable medium. The boundary between the media is modelled as a hard wall or a free surface. Assuming that the surface is a hard or soft wall simplifies the calculations, as there will be no absorption and all incident intensity will be reflected, i.e. a reflecting boundary condition. The surface is illuminated by a Gaussian beam propagating towards the lower medium.

The system is described in a three-dimensional coordinate system, with vacuum in the region $x_3 > \zeta(\boldsymbol{x}_\parallel)$ and the non-penetrable medium in the region $x_3 < \zeta(\boldsymbol{x}_\parallel)$. The surface profile is described as $x_3 = \zeta(\boldsymbol{x}_\parallel)$, where $\boldsymbol{x}_\parallel$ is the projection of $\boldsymbol{x}$ onto the x_1x_2-plane. The surface function is assumed to be a single-valued function of $\boldsymbol{x}_\parallel$. The surface profile function has a Gaussian height distribution and a Gaussian correlation function with a correlation length along the x_1- and x_2-axis.

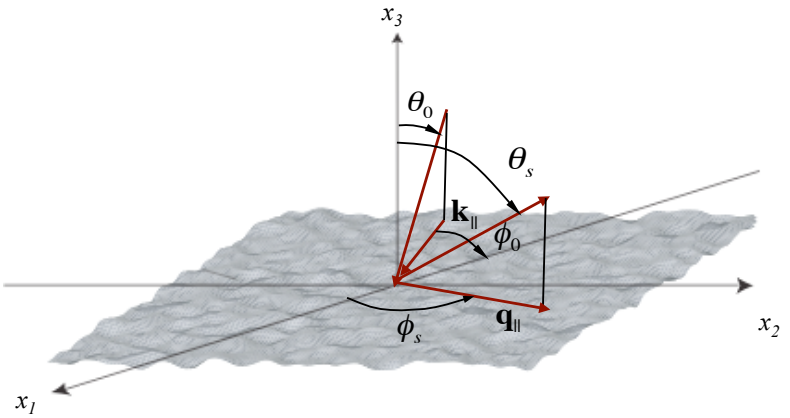

Figure 2.1: Scattering geometry for the rough surface interface. Angles of incidence ϕ_0 and θ_0, and scattering ϕ_s and θ_s are shown. (Image from Ref. [12].)

The scattering geometry is described by the polar and azimuthal angles, for the incident wave ϕ_0 and θ_0, and similarly for the scattered wave ϕ_s and θ_s, Fig. 2.1. This also defines the wave vectors for the incident and scattered beam, $\boldsymbol{k}$ and $\boldsymbol{q}$, given by

$$\boldsymbol{k} = \frac{\omega}{c}\left(\sin(\theta_0)\cos(\phi_0), \sin(\theta_0)\sin(\phi_0), -\cos(\theta_0)\right), \tag{2.1}$$

$$\boldsymbol{q} = \frac{\omega}{c}\left(\sin(\theta_s)\cos(\phi_s), \sin(\theta_s)\sin(\phi_s), \cos(\theta_s)\right). \tag{2.2}$$

Projected onto the x_1x_2-plane, $\boldsymbol{k}$ and $\boldsymbol{q}$ give the component of the wave vector along the surface, $\boldsymbol{k}_\parallel$ and $\boldsymbol{q}_\parallel$.

2.2 Randomly rough surfaces

All surfaces have some kind of structure, varying from smooth for all practical purposes to strongly rough. In classifying a surface as rough, one has to determine what is considered rough. All surfaces are rough on some scale, and more complex systems can be seen as a combination of, possibly many, plane surfaces. Rough surfaces can have a periodic structure, one example is sinusoidal surfaces, for which scattering has been studied analytically. Surfaces created by a random process will not have a defined periodicity, but will be similar in the sense that they are generated from the same process. If one measures the height on a fine grid over the surface, the surface structure can be found. In most cases, the process that created the surface has some kind of correlation between surface points close to each other. The height of the surface will follow a correlation function, the height of the surface on a given point will depend on the height at nearby points. We will focus on correlated surfaces.

Surface topography is not enough to decide what process generated the surface. Each realisation is different, but surfaces generated from the same underlying process shares the statistics describing the surface. Probing the statistics of the surface rather than the structure of one realisation requires averaging over many samples. Gaussian statistics simplifies calculation and gives a good approximation to many real surfaces. The structure of the roughness depends on the process that created the interface, but in many cases the structure can be approximated by a Gaussian height distribution.

A one-dimensional surface is extended along the x_1-axis, and has a surface profile in the x_3-direction, described by a surface profile function $\zeta(x_1)$. For two-dimensional surfaces, this is expanded to a surface along the x_1x_2-plane with a height in the x_3-direction. The surface is described by a surface profile function, $x_3 = \zeta(\boldsymbol{x}_\parallel)$, that gives the height of the surface above a reference plane at the lateral coordinate $\boldsymbol{x}_\parallel = (x_1, x_2, 0)$.

We consider surfaces which on average are planar, that is, the structure can be considered as fluctuations around zero, $\langle\zeta(\boldsymbol{x}_\parallel)\rangle = 0$. It is assumed that the surface does not have overhangs, that is, the surface profile function $\zeta(\boldsymbol{x}_\parallel)$ is a single valued function of $\boldsymbol{x}_\parallel$. If this is not the case, one can no longer do the integration over the x_1x_2-plane, but must integrate over the surface using a parametric representation [5, 6].

The relation between surface points is, given that the surface function $\zeta(\boldsymbol{x}_\parallel)$ is stationary,

$$\langle \zeta(\boldsymbol{x}_\parallel)\zeta(\boldsymbol{x}'_\parallel)\rangle = \delta^2 W(\boldsymbol{x}_\parallel - \boldsymbol{x}'_\parallel), \tag{2.3}$$

where δ denotes the RMS-height defined as $\delta = \langle \zeta^2(x_1)\rangle^{\frac{1}{2}}$ and W is the correlation function, normalised so that $W(0) = 1$. The isotropic Gaussian correlation function can be written as

$$W(\boldsymbol{x}_\parallel) = \exp\left[-\frac{|\boldsymbol{x}_\parallel|^2}{a^2}\right] = \exp\left[-\frac{x_1^2 + x_2^2}{a^2}\right], \tag{2.4}$$

where a is the correlation length. We can define a mean slope as

$$s \approx \frac{\delta}{a}, \tag{2.5}$$

RMS-roughness over correlation length, as the RMS-roughness is a measure of the movement in the x_3 direction and the correlation length a length in the x_1x_2-plane.

The power spectrum of the surface profile, defined as the Fourier transform of the correlation function, reads

$$g(\boldsymbol{k}_\parallel) = \int \mathrm{d}^2 x_\parallel \; W(\boldsymbol{x}_\parallel) \exp(-i\boldsymbol{k}_\parallel \cdot \boldsymbol{x}_\parallel). \tag{2.6}$$

It is used to describe the surface roughness, and often appears when describing the scattering process, e.g. in perturbation theory.

2.2.1 Anisotropic surfaces

Surfaces that exhibit different properties in different directions are said to be anisotropic. The anisotropy of the structure is assumed to be described as two correlation lengths along perpendicular axis, oriented such that the direction of the shortest and longest correlation lengths corresponds to the x_1 and x_2 axis respectively.

The two-dimensional, Gaussian correlation function describing the anisotropic surface is given by

$$W(\boldsymbol{x}_\parallel) = \exp\left[-\frac{x_1^2}{a_1^2} - \frac{x_2^2}{a_2^2}\right], \tag{2.7}$$

where a_1 is the correlation length along the x_1-axis and equivalently a_2 along the x_2-axis [12].

2.2.2 Self-affine surfaces

A surface is self-affine, between the scales ξ_- and ξ_+, if it remains statistically invariant in this region under the transformation

$$\Delta\boldsymbol{x}_\parallel \to \Lambda\Delta\boldsymbol{x}_\parallel, \tag{2.8}$$

$$\Delta\zeta \to \Lambda^H \Delta\zeta, \tag{2.9}$$

for all positive, real numbers Λ. In Eq. (2.9) H denotes the Hurst exponent that characterises the invariance.

The Hurst exponent is usually in the range $0 < H < 1$. When $H = 1/2$ the surface is an example of a random (Brownian) walk with uncorrelated increments. If $H > 1/2$ the profile is correlated, that is, the next step is more likely to be in the same direction as the previous step. If $H < 1/2$ the profile is said to be anti-correlated, a step in one direction is more likely to be followed by a step in the opposite direction.

The difference vector is defined as

$$\Delta \boldsymbol{x}_{\parallel} = \boldsymbol{x}_{\parallel} - \boldsymbol{x}'_{\parallel}. \tag{2.10}$$

The scaling relation can be rewritten in an equivalent, more compact form

$$\Delta\zeta(\Delta \boldsymbol{x}_{\parallel}) \approx \Lambda^{-H} \Delta\zeta(\Lambda \Delta \boldsymbol{x}_{\parallel}). \tag{2.11}$$

We introduce the RMS-value of the height-difference, measured over a window $\Delta \boldsymbol{x}_{\parallel}$,

$$\sigma(\Delta \boldsymbol{x}_{\parallel}) = \left\langle [\zeta(\boldsymbol{x}_{\parallel}) - \zeta(\boldsymbol{x}'_{\parallel})]^2 \right\rangle^{1/2}. \tag{2.12}$$

For an isotropic surface, the difference vector is independent of the direction in the surface plane,

$$\sigma(\Delta \boldsymbol{x}_{\parallel}) = \sigma(|\Delta \boldsymbol{x}_{\parallel}| = \Delta x_{\parallel}). \tag{2.13}$$

With this definition, the topothesy is defined as the length scale, ℓ, over which

$$\sigma(\ell) = \ell. \tag{2.14}$$

From Eq. (2.12) we have that $\sigma(\Delta x_{\parallel}) \sim x_{\parallel}^H$, and by using Eq. (2.14) we get

$$\sigma(\Delta x_{\parallel}) = \ell^{1-H} \Delta x_{\parallel}^H. \tag{2.15}$$

From the scaling relation for the surface, Eq. (2.9) , one can find the scaling relation for of the power spectrum of the surface. This can be used for generating self-affine surfaces with a given Hurst exponent. For a two-dimensional, quadratic surface of length L, the power spectrum is, according to the Wiener-Khinchin theorem, defined as

$$g(|\boldsymbol{k}_{\parallel}|) = \frac{1}{L^2} \int \mathrm{d}^2 x_{\parallel}\, e^{i \boldsymbol{k}_{\parallel} \boldsymbol{x}_{\parallel}} \left\langle \zeta(\boldsymbol{y}_{\parallel} + \boldsymbol{x}_{\parallel}) \zeta(\boldsymbol{y}_{\parallel}) \right\rangle_{\boldsymbol{y}_{\parallel}}, \tag{2.16}$$

where $\left\langle \zeta(\boldsymbol{y}_{\parallel} + \boldsymbol{x}_{\parallel}) \zeta(\boldsymbol{y}_{\parallel}) \right\rangle_{\boldsymbol{y}_{\parallel}}$ is the (two-point) correlation function. By taking advantage of the scaling equations, Eqs. (2.9) and (2.11), one finds

$$g\left(\left|\frac{\boldsymbol{k}_{\parallel}}{\Lambda}\right|\right) \simeq \frac{1}{(\Lambda L)^2} \int \mathrm{d}^2(\Lambda x_{\parallel})\, e^{i \boldsymbol{k}_{\parallel} \boldsymbol{x}_{\parallel}} \left\langle \Lambda^H \zeta(\boldsymbol{y}_{\parallel} + \boldsymbol{x}_{\parallel}) \Lambda^H \zeta(\boldsymbol{y}_{\parallel}) \right\rangle_{\boldsymbol{y}_{\parallel}}. \tag{2.17}$$

From Eq. (2.17) one obtains

$$g\left(\left|\frac{\boldsymbol{k}_{\parallel}}{\Lambda}\right|\right) \simeq \Lambda^{2H+2} g(|\boldsymbol{k}_{\parallel}|), \tag{2.18}$$

so that the power spectrum has to scale like

$$g(|\boldsymbol{k}_{\parallel}|) \sim \boldsymbol{k}_{\parallel}^{-2H-2}. \tag{2.19}$$

Introducing the mean slope, we have that the standard deviation of the surface profile over an interval $\Delta x_{\parallel}$ denotes a height-difference over the interval. This gives a mean slope of

$$s(\Delta x_{\parallel}) = \frac{\sigma(\Delta x_{\parallel})}{\Delta x_{\parallel}} = \left(\frac{\ell}{\Delta x_{\parallel}}\right)^{H-1}. \tag{2.20}$$

With $\Delta x_{\parallel} = \lambda$, this gives

$$s(\lambda) = \left(\frac{\ell}{\lambda}\right)^{H-1}, \tag{2.21}$$

which will be used when classifying the self-affine surfaces.

2.3 Acoustic waves

The wave equation in an ideal fluid can be derived from the equation for conservation of mass, Euler's equation and the adiabatic equation of state [4],

$$\frac{\partial \rho}{\partial t} = -\nabla \cdot \rho \boldsymbol{v}, \tag{2.22}$$

$$\frac{\partial \boldsymbol{v}}{\partial t} + \boldsymbol{v} \cdot \nabla \boldsymbol{v} = -\frac{1}{\rho} \nabla p(\rho), \tag{2.23}$$

$$p = p_0 + \rho' \left[\frac{\partial p}{\partial \rho}\right]_S + \frac{1}{2}(\rho')^2 \left[\frac{\partial^2 p}{\partial \rho^2}\right]_S + \ldots, \tag{2.24}$$

respectively. We also define the quantity

$$c^2 \equiv \left[\frac{\partial p}{\partial \rho}\right]_S, \tag{2.25}$$

where c is the speed of sound, ρ the density, $\boldsymbol{v}$ the particle velocity, p the pressure and the subscript S denotes the thermodynamic partial derivatives taken at constant entropy. The ambient quantities of the time independent medium are identified by the subscript 0. We use small perturbations for the pressure and density, $p = p_0 + p'$, $\rho = \rho_0 + \rho'$.

The linear linear approximation retaining only first-order terms of Eqs. (2.22), (2.23) and (2.24) gives

$$\frac{\partial \rho'}{\partial t} = -\rho_0 \nabla \cdot \boldsymbol{v}, \tag{2.26}$$

$$\frac{\partial \boldsymbol{v}}{\partial t} = \frac{1}{\rho_0} \nabla p'(\rho), \tag{2.27}$$

$$p' = \rho' c^2. \tag{2.28}$$

We assume that the material properties ρ_0 and c^2 are independent of time. We take the divergence of Eq. (2.26) and the time derivative of Eq. (2.27), and combine them using (2.28), giving

$$\frac{1}{\rho} \nabla \left(\rho c^2 \nabla \cdot \boldsymbol{v} \right) - \frac{\partial^2 \boldsymbol{v}}{\partial t^2} = \boldsymbol{0}. \tag{2.29}$$

If the density is constant or slowly varying, Eq. (2.29) can be transformed into a scalar wave equation for the velocity potential by introducing the velocity potential ψ, defined by

$$\boldsymbol{v} = \nabla \psi. \tag{2.30}$$

Substituting Eq. (2.30) and the constant density condition, $\nabla \rho = \boldsymbol{0}$, into Eq. (2.29), the latter takes the form

$$\nabla \left(c^2 \nabla^2 \psi - \frac{\partial^2 \psi}{\partial t} \right) = \boldsymbol{0}. \tag{2.31}$$

Eq. (2.31) is satisfied if ψ satisfies the simple wave equation

$$\nabla^2 \psi - \frac{1}{c^2} \frac{\partial^2 \psi}{\partial t} = 0. \tag{2.32}$$

A source in the region can be represented as a right hand side in Eq. (2.32) on the form $f(\boldsymbol{x}|t)$, giving an inhomogeneous wave equation.

Since the coefficients to the two differential operators in Eq. (2.32) are independent of time, the dimension of the wave equation can be reduced to three by using the frequency-time Fourier transform pair, giving the frequency-domain wave equation, or Helmholtz equation,

$$\left[\nabla^2 + \left(\frac{\omega}{c(\boldsymbol{x})} \right)^2 \right] \psi(\boldsymbol{x}|\omega) = f(\boldsymbol{x}|\omega). \tag{2.33}$$

where ω is the angular frequency of the field and c the sound velocity. We define the wave number $k(\boldsymbol{x}) = \frac{\omega}{c(\boldsymbol{x})}$. For homogeneous media where the speed of sound is position independent, this reduces to $k = \frac{\omega}{c}$.

For a domain without sources, $f(\boldsymbol{x}|\omega) = 0$, the Helmholtz equation reduces to

$$\left[\nabla^2 + k(\boldsymbol{x})^2 \right] \psi(\boldsymbol{x}|\omega) = 0. \tag{2.34}$$

2.4 Scalar beam scattering from a two-dimensional surface

We will now apply the frequency domain wave equation to the system described in Sec. 2.1. That is, a system consisting of a two-dimensional boundary generated by a random process, $x_3 = \zeta(\boldsymbol{x}_\parallel)$, modelled as a hard wall, Neumann, boundary condition[18] or a free surface, Dirichlet, boundary condition[17] separating a medium supporting propagating waves in the region $x_3 > \zeta(\boldsymbol{x}_\parallel)$ and a non-penetrable medium in the region $x_3 < \zeta(\boldsymbol{x}_\parallel)$.

The field in the upper region, $\psi(\boldsymbol{x}|\omega)$ is a solution of the Helmholtz equation, Eq. (2.33),

$$\left[\nabla^2 + \left(\frac{\omega}{c}\right)^2\right] \psi(\boldsymbol{x}|\omega) = 0,\ x_3 > \zeta(\boldsymbol{x}_\parallel). \tag{2.35}$$

2.4.1 Surface boundary conditions

The field satisfies either the Dirichlet boundary condition if

$$\psi(\boldsymbol{x}|\omega)\big|_{x_3=\zeta(\boldsymbol{x}_\parallel)} = 0, \tag{2.36}$$

zero pressure at the surface, free surface/soft wall, or the Neumann boundary condition if

$$\partial_n \psi(\boldsymbol{x}|\omega)\big|_{x_3=\zeta(\boldsymbol{x}_\parallel)} = 0, \tag{2.37}$$

zero normal velocity at the surface, hard wall. In Eq. (2.37) ∂_n is the derivative normal to the surface, directed into the vacuum, $\partial_n \equiv \hat{n} \cdot \nabla$.

We introduce the Green's function of the Helmholtz equation, Eq. (2.33), $g_0(\boldsymbol{x}|\boldsymbol{x'})$, satisfying

$$\left[\nabla^2 + \left(\frac{\omega}{c}\right)^2\right] g_0(\boldsymbol{x}|\boldsymbol{x}') = -4\pi\delta(\boldsymbol{x} - \boldsymbol{x'}). \tag{2.38}$$

The Green's function can be represented as

$$\begin{aligned} g_0(\boldsymbol{x}|\boldsymbol{x}') &= \frac{\exp\left[i\frac{\omega}{c} \mid \boldsymbol{x} - \boldsymbol{x}' \mid\right]}{\mid \boldsymbol{x} - \boldsymbol{x}' \mid} \\ &= \int \frac{\mathrm{d}^2 k_\parallel}{(2\pi)^2} \frac{2\pi i}{\alpha_0(k_\parallel)} \exp[i\boldsymbol{k}_\parallel \cdot (\boldsymbol{x}_\parallel - \boldsymbol{x}'_\parallel)] \cdot \exp[i\alpha_0(k_\parallel) \mid x_3 - x'_3 \mid], \end{aligned} \tag{2.39}$$

where α_0 is defined as

$$\alpha_0(k_\parallel) = \begin{cases} \sqrt{\left(\frac{\omega}{c}\right)^2 - k_\parallel^2}, & k_\parallel^2 < \omega^2/c^2, \\ i\sqrt{k_\parallel^2 - \left(\frac{\omega}{c}\right)^2}, & k_\parallel^2 > \omega^2/c^2. \end{cases} \tag{2.40}$$

We apply Green's second integral identity [3]

$$\int_{\Omega} \mathrm{d}^2x \, (u\nabla^2 v - v\nabla^2 u) = \int_{\sum} \mathrm{d}S \, (u\partial_\nu v - v\partial_\nu u)\,, \tag{2.41}$$

where $u(\boldsymbol{x})$ and $v(\boldsymbol{x})$ are arbitrary scalar functions of $\boldsymbol{x}$, defined in a volume Ω bounded by a closed surface $\sum$. The derivative ∂_ν is taken along the normal to the surface $\sum$, directed away from the volume Ω. We set Ω to be the region $x_3 > \zeta(\boldsymbol{x}_\parallel)$ and $\sum$ to the union of the surface $x_3 = \zeta(\boldsymbol{x}_\parallel)$, denoted S, and a hemispherical cap of infinite radius in the upper half-space, denoted $S^{(+\infty)}$. Then, setting $u = \psi(\boldsymbol{x}|\omega)$ and $v = g_0(\boldsymbol{x}|\boldsymbol{x}')$ in Eq. (2.41) and using Eqs. (2.35) and (2.38), we obtain

$$\begin{aligned} -4\pi\theta(x_3' - \zeta(\boldsymbol{x}_\parallel'))\psi(\boldsymbol{x}'|\omega) = &- \int_S \mathrm{d}S \, [\psi(\boldsymbol{x}|\omega)\partial_n g_0(\boldsymbol{x}|\boldsymbol{x}') - g_0(\boldsymbol{x}|\boldsymbol{x}')\partial_n \psi(\boldsymbol{x}|\omega)] \\ &+ \int_{S^{(+\infty)}} \mathrm{d}S \, [\psi(\boldsymbol{x}|\omega)\partial_\nu g_0(\boldsymbol{x}|\boldsymbol{x}') - g_0(\boldsymbol{x}|\boldsymbol{x}')\partial_\nu \psi(\boldsymbol{x}|\omega)], \end{aligned} \tag{2.42}$$

where $\theta(x)$ is the Heaviside step function. As the scattered field will satisfy a radiation condition at infinity, its contribution to the surface integral over $S^{(+\infty)}$ vanishes. The second term of the right hand side of Eq. (2.42) therefore yields $-4\pi\psi(\boldsymbol{x}|\omega)_{\mathrm{inc}}$, where $\psi(\boldsymbol{x}|\omega)_{\mathrm{inc}}$ is the incident field. Eq. (2.42) can then be rewritten as

$$\begin{aligned} \theta(x_3 - \zeta(\boldsymbol{x}_\parallel))\psi(\boldsymbol{x}|\omega) = \psi(\boldsymbol{x}|\omega)_{\mathrm{inc}} + \frac{1}{4\pi}\int_S \mathrm{d}S' \, [\, &(\partial_{n'} g_0(\boldsymbol{x}|\boldsymbol{x}'))\, \psi(\boldsymbol{x}'|\omega) \\ &- g_0(\boldsymbol{x}|\boldsymbol{x}')\partial_{n'}\psi(\boldsymbol{x}'|\omega)], \end{aligned} \tag{2.43}$$

having used that $g_0(\boldsymbol{x}|\boldsymbol{x}')$ is symmetric in $\boldsymbol{x}$ and $\boldsymbol{x}'$.

When the surface profile function $\zeta(\boldsymbol{x}_\parallel)$ is a single valued function, the integration over the surface S can be replaced with an integration over the plane $x_3 = 0$,

$$\begin{aligned} \theta(x_3 - \zeta(\boldsymbol{x}_\parallel))\psi(\boldsymbol{x}|\omega) = \psi(\boldsymbol{x}|\omega)_{\mathrm{inc}} + \frac{1}{4\pi}\int \mathrm{d}^2x_\parallel' \, \{ &[\partial_{N'} g_0(\boldsymbol{x}|\boldsymbol{x}')]\big|_{x_3' = \zeta(\boldsymbol{x}_\parallel')} \mathcal{F}(\boldsymbol{x}_\parallel'|\omega) \\ &- [g_0(\boldsymbol{x}|\boldsymbol{x}')]\big|_{x_3' = \zeta(\boldsymbol{x}_\parallel')} \mathcal{N}(\boldsymbol{x}_\parallel'|\omega)\}, \end{aligned} \tag{2.44}$$

introducing the notation

$$\partial_N = -\partial_{x_1}\zeta(\boldsymbol{x}_\parallel)\partial_{x_1} - \partial_{x_2}\zeta(\boldsymbol{x}_\parallel)\partial_{x_2} + \partial_{x_3}, \tag{2.45}$$

and defining the source functions

$$\mathcal{F}(\boldsymbol{x}_\parallel|\omega) = \psi(\boldsymbol{x}|\omega)\big|_{x_3 = \zeta(\boldsymbol{x}_\parallel)}, \tag{2.46}$$

$$\mathcal{N}(\boldsymbol{x}_\parallel|\omega) = \partial_N \psi(\boldsymbol{x}|\omega)\big|_{x_3 = \zeta(\boldsymbol{x}_\parallel)}. \tag{2.47}$$

2.4.2 Dirichlet boundary condition

When the field satisfies the Dirichlet boundary condition at the surface, Eq. (2.44) becomes

$$\theta(x_3 - \zeta(\boldsymbol{x}_\parallel))\psi(\boldsymbol{x}|\omega) = \psi(\boldsymbol{x}|\omega)_{\text{inc}} - \frac{1}{4\pi}\int \mathrm{d}^2 x'_\parallel \, [g_0(\boldsymbol{x}|\boldsymbol{x}')]\big|_{x'_3=\zeta(\boldsymbol{x}'_\parallel)} \mathcal{N}(\boldsymbol{x}'_\parallel|\omega). \tag{2.48}$$

The scattered field is given by

$$\psi(\boldsymbol{x}|\omega)_{\text{sc}} = -\frac{1}{4\pi}\int \mathrm{d}^2 x'_\parallel \, [g_0(\boldsymbol{x}|\boldsymbol{x}')]\big|_{x'_3=\zeta(\boldsymbol{x}'_\parallel)} \mathcal{N}(\boldsymbol{x}'_\parallel|\omega). \tag{2.49}$$

In the far field region this can be rewritten as, using Eq. (2.39),

$$\psi(\boldsymbol{x}|\omega)_{\text{sc}} = \int \frac{\mathrm{d}^2 q_\parallel}{(2\pi)^2} \, R_D(\boldsymbol{q}_\parallel, \omega) \exp[i\boldsymbol{q}_\parallel \cdot \boldsymbol{x}_\parallel + i\alpha_0(q_\parallel)x_3]. \tag{2.50}$$

This gives an expression for the scattering amplitude,

$$R_D(\boldsymbol{q}_\parallel, \omega) = \frac{-i}{2\alpha_0(q_\parallel)} \int \mathrm{d}^2 x_\parallel \, \mathcal{N}(\boldsymbol{x}_\parallel|\omega) \exp[-i\boldsymbol{q}_\parallel \cdot \boldsymbol{x}_\parallel - i\alpha_0(q_\parallel)x_3]. \tag{2.51}$$

2.4.3 Neumann boundary condition

Alternatively, if the field satisfies the Neumann boundary condition at the surface, Eq. (2.44) becomes

$$\theta(x_3 - \zeta(\boldsymbol{x}_\parallel))\psi(\boldsymbol{x}|\omega) = \psi(\boldsymbol{x}|\omega)_{\text{inc}} + \frac{1}{4\pi}\int \mathrm{d}^2 x'_\parallel \, [\partial_{N'} g_0(\boldsymbol{x}|\boldsymbol{x}')]\big|_{x'_3=\zeta(\boldsymbol{x}'_\parallel)} \mathcal{F}(\boldsymbol{x}'_\parallel|\omega). \tag{2.52}$$

The scattered field is given by

$$\psi(\boldsymbol{x}|\omega)_{\text{sc}} = \frac{1}{4\pi}\int \mathrm{d}^2 x'_\parallel \, [\partial_{N'} g_0(\boldsymbol{x}|\boldsymbol{x}')]\big|_{x'_3=\zeta(\boldsymbol{x}'_\parallel)} \mathcal{F}(\boldsymbol{x}'_\parallel|\omega). \tag{2.53}$$

In the far field region this can be rewritten as, using Eq. (2.38),

$$\psi(\boldsymbol{x}|\omega)_{\text{sc}} = \int \frac{\mathrm{d}^2 q_\parallel}{(2\pi)^2} \, R_N(\boldsymbol{q}_\parallel, \omega) \exp[i\boldsymbol{q}_\parallel \cdot \boldsymbol{x}_\parallel + i\alpha_0(q_\parallel)x_3]. \tag{2.54}$$

This is the same expression as for the Dirichlet boundary condition Eq. (2.50), except the scattering amplitude now being

$$R_N(\boldsymbol{q}_\parallel, \omega) = \frac{-1}{2\alpha_0(q_\parallel)} \int \mathrm{d}^2 x_\parallel \, \mathcal{F}(\boldsymbol{x}_\parallel|\omega)[\boldsymbol{q}_\parallel \cdot \nabla\zeta(\boldsymbol{x}_\parallel) - \alpha_0(q_\parallel)] \cdot \exp[-i\boldsymbol{q}_\parallel \cdot \boldsymbol{x}_\parallel - i\alpha_0(q_\parallel)x_3]. \tag{2.55}$$

2.4.4 Incident field

The incident field satisfies the Helmholtz equation

$$\left[\nabla^2 + \left(\frac{\omega}{c}\right)^2\right] \psi(\boldsymbol{x}|\omega)_{\text{inc}} = 0. \tag{2.56}$$

An incident beam of limited width is created by limiting incident plane waves with a Gaussian weight function,

$$\psi(\boldsymbol{x}|\omega)_{\text{inc}} = \frac{w^2}{2\pi} \int\limits_{q_\parallel < \frac{\omega}{c}} \mathrm{d}^2 q_\parallel \, e^{i\boldsymbol{q}_\parallel \cdot \boldsymbol{x}_\parallel - i\alpha_0(q_\parallel)x_3} e^{-\frac{w^2}{2}(\boldsymbol{q}_\parallel - \boldsymbol{k}_\parallel)^2}, \tag{2.57}$$

with a half width of w and where $\boldsymbol{k}_\parallel$ is the projection of the wave vector of the incident light, $\boldsymbol{k}$, onto the $x_3 = 0$ plane.

2.4.5 Differential reflection coefficient

The total scattered flux crossing a plane above $x_3 = \zeta(\boldsymbol{x}_\parallel)_{\max}$ is written as

$$\begin{aligned}
P_{\text{sc}} =& \frac{\hbar}{m} \Im \int \mathrm{d}^2 x_\parallel \, \psi^*(\boldsymbol{x})_{\text{sc}} \partial_{x_3} \psi(\boldsymbol{x})_{\text{sc}} \\
=& \frac{\hbar}{m} \Im \int \mathrm{d}^2 x_\parallel \int \frac{\mathrm{d}^2 q_\parallel}{(2\pi)^2} \, R^*(\boldsymbol{q}_\parallel, \omega) e^{-i\boldsymbol{q}_\parallel \cdot \boldsymbol{x}_\parallel} e^{-i\alpha_0^*(q_\parallel)x_3} \\
& \cdot \int \frac{\mathrm{d}^2 q'_\parallel}{(2\pi)^2} \, i\alpha_0(q'_\parallel) R(\boldsymbol{q}'_\parallel, \omega) e^{i\boldsymbol{q}'_\parallel \cdot \boldsymbol{x}_\parallel} e^{i\alpha_0(q'_\parallel)x_3} \\
=& \frac{\hbar}{m} \Im \int \frac{\mathrm{d}^2 q_\parallel}{(2\pi)^2} \, i\alpha_0(q_\parallel) |R(\boldsymbol{q}_\parallel, \omega)|^2 e^{-2\Im\alpha_0(q_\parallel)x_3} \\
=& \frac{\hbar}{m} \int\limits_{q_\parallel < \frac{\omega}{c}} \frac{\mathrm{d}^2 q_\parallel}{(2\pi)^2} \, \alpha_0(q_\parallel) |R(\boldsymbol{q}_\parallel, \omega)|^2.
\end{aligned} \tag{2.58}$$

The scattering amplitude $R(\boldsymbol{q}_\parallel, \omega)$ is either the Dirichlet scattering amplitude, $R_D(\boldsymbol{q}_\parallel, \omega)$, or the Neumann scattering amplitude, $R_N(\boldsymbol{q}_\parallel, \omega)$. The surface parallel wave vector, $\boldsymbol{q}_\parallel$, can be written in terms of the polar and azimuthal scattering angles, θ_s and ϕ_s, as

$$\boldsymbol{q}_\parallel = \frac{\omega}{c} \sin\theta_s (\cos\phi_s, \sin\phi_s, 0). \tag{2.59}$$

This gives

$$\alpha_0(q_\parallel, \omega) = \frac{\omega}{c} \cos\theta_s, \tag{2.60}$$

$$\mathrm{d}^2 q_\parallel = \left(\frac{\omega}{c}\right)^2 \cos\theta_s \mathrm{d}\Omega_s. \tag{2.61}$$

$$\tag{2.62}$$

Here $\mathrm{d}\Omega_s = \sin\theta_s \mathrm{d}\theta_s \mathrm{d}\phi_s$ is the element of solid angle around the direction (θ_s, ϕ_s). The total scattered flux can be written as

$$P_{\mathrm{sc}} = \int \mathrm{d}\Omega_s \, p_{\mathrm{sc}}(\Omega_s), \tag{2.63}$$

where

$$p_{\mathrm{sc}}(\Omega_s) = \frac{\hbar}{m} \left(\frac{\omega}{2\pi c}\right)^2 \frac{\omega}{c} \cos^2\theta_s \left| R(\boldsymbol{q}_\parallel, \omega) \right|^2 . \tag{2.64}$$

The scattered flux, (2.64) must be normalized by the magnitude of the total incident flux to obtain the differential reflection coefficient. The total time-averaged incident flux takes the form

$$\begin{aligned} P_{\mathrm{inc}} =& \left| \frac{\hbar}{m} \Im \int \mathrm{d}^2 x_\parallel \, \psi^*(\boldsymbol{x})_{\mathrm{inc}} \partial_{x_3} \psi(\boldsymbol{x})_{\mathrm{inc}} \right| \\ =& \frac{\hbar}{m} \Bigg| \Im \int \mathrm{d}^2 x_\parallel \, \frac{w}{2\pi} \int\limits_{q_\parallel < \frac{w}{c}} \mathrm{d}^2 q_\parallel \, e^{-i\boldsymbol{q}_\parallel \cdot \boldsymbol{x}_\parallel} e^{i\alpha_0^*(q_\parallel) x_3} e^{-\frac{w^2}{2}(\boldsymbol{q}_\parallel - \boldsymbol{k}_\parallel)^2} \\ & \cdot \frac{w}{2\pi} \int\limits_{q'_\parallel < \frac{w}{c}} \mathrm{d}^2 q'_\parallel \, (-i\alpha_0(q'_\parallel)) e^{i\boldsymbol{q}'_\parallel \cdot \boldsymbol{x}_\parallel} e^{i\alpha_0(q'_\parallel) x_3} e^{-\frac{w^2}{2}(\boldsymbol{q}'_\parallel - \boldsymbol{k}_\parallel)^2} \Bigg| \\ =& \frac{\hbar}{m} w^4 \int\limits_{q_\parallel < \frac{\omega}{c}} \mathrm{d}^2 q_\parallel \, \alpha_0(q_\parallel) e^{-w^2(\boldsymbol{q}_\parallel - \boldsymbol{k}_\parallel)^2} . \end{aligned} \tag{2.65}$$

The integral can be rewritten as

$$P_{\mathrm{inc}} = \frac{\hbar}{m} 2\pi w^4 \frac{\omega}{c}^3 e^{-w^2 k_\parallel^2} \int_0^{\frac{\pi}{2}} \mathrm{d}\theta \, \sin\theta \cos^2\theta \cdot I_0 \left(2w^2 \frac{\omega}{c} k_\parallel \sin\theta\right) e^{-w^2 \frac{\omega^2}{c^2} \sin^2\theta}, \tag{2.66}$$

where I_0 is the modified Bessel function of the first kind and zero order. This is the same expression as for the EM wave, where it was obtained from the Poynting vector[10], except from the factor $\hbar/m$ in Eq. (2.57) for the scalar wave. The differential reflection coefficient is then given by

$$\frac{\partial R}{\partial \Omega_s} = \frac{1}{(2\pi)^2} \frac{\hbar}{m} \left(\frac{\omega}{c}\right)^3 \frac{\cos^2\theta_s}{P_{\mathrm{inc}}} \left| R(\boldsymbol{q}_\parallel, \omega) \right|^2 . \tag{2.67}$$

Averaging this over an ensemble of surface realizations, we obtain the mean differential reflection coefficient (MDRC). If the scattered field is averaged over many surface realizations, the coherent component remains, and the diffuse component cancels due to its random phase with respect to the incident field. If the field intensity is averaged instead, both components remain. The MDRC is split into an incoherent and a coherent part, using Eq. (3.6). The incoherent part is

$$\left\langle \frac{\partial R}{\partial \Omega_s} \right\rangle_{\mathrm{incoh}} = \frac{1}{(2\pi)^2} \frac{\hbar}{m} \left(\frac{\omega}{c}\right)^3 \frac{\cos^2\theta_s}{P_{\mathrm{inc}}} \left[\left\langle \left| R(\boldsymbol{q}_\parallel, \omega) \right|^2 \right\rangle - \left| \left\langle R(\boldsymbol{q}_\parallel, \omega) \right\rangle \right|^2 \right], \tag{2.68}$$

and the coherent part

$$\left\langle \frac{\partial R}{\partial \Omega_s} \right\rangle_{\mathrm{coh}} = \frac{1}{(2\pi)^2} \frac{\hbar}{m} \left(\frac{\omega}{c}\right)^3 \frac{\cos^2\theta_s}{P_{\mathrm{inc}}} \left| \left\langle R(\boldsymbol{q}_\parallel, \omega) \right\rangle \right|^2 . \tag{2.69}$$

2.4.6 Equations satisfied by the source functions

2.4.6.1 Neumann boundary condition

We evaluate Eq. (2.52) at $x_3 = \zeta(\boldsymbol{x}_\parallel) + \eta$ and $x_3 = \zeta(\boldsymbol{x}_\parallel) - \eta$ and add the resulting equations,

$$\mathcal{F}(\boldsymbol{x}_\parallel|\omega) = 2\mathcal{F}^{(i)}(\boldsymbol{x}_\parallel|\omega) - \frac{1}{2\pi}\mathrm{P}\int \mathrm{d}^2x_\parallel \, [\![\partial_{N'} g_0(\boldsymbol{x}|\boldsymbol{x}')]\!]\mathcal{F}(\boldsymbol{x}'_\parallel|\omega), \tag{2.70}$$

letting $\eta \to 0^+$, where P denotes the Cauchy principal value and the notation $[\![f(\boldsymbol{x}|\boldsymbol{x}')]\!] = f(\boldsymbol{x}|\boldsymbol{x}')\Big|_{\substack{x_3=\zeta(\boldsymbol{x}_\parallel)\\ x'_3=\zeta(\boldsymbol{x}'_\parallel)}}$ is used. The incident field is defined by

$$\mathcal{F}^{(i)}(\boldsymbol{x}_\parallel|\omega) = \psi(\boldsymbol{x}|\omega)_{\mathrm{inc}}\big|_{x_3=\zeta(\boldsymbol{x}_\parallel)}. \tag{2.71}$$

In Eq. (2.70) we have also used that

$$\partial_{N'} g_0(\boldsymbol{x}|\boldsymbol{x}')\Big|_{\substack{x'_3=\zeta(\boldsymbol{x}'_\parallel)\\ x_3=\zeta(\boldsymbol{x}_\parallel)+\eta}} + \partial_{N'} g_0(\boldsymbol{x}|\boldsymbol{x}')\Big|_{\substack{x'_3=\zeta(\boldsymbol{x}'_\parallel)\\ x_3=\zeta(\boldsymbol{x}_\parallel)-\eta}} = \begin{cases} [\![\partial_{N'} g_0(\boldsymbol{x}|\boldsymbol{x}')]\!] & \boldsymbol{x}_\parallel \neq \boldsymbol{x}'_\parallel \\ 0 & \boldsymbol{x}_\parallel = \boldsymbol{x}'_\parallel \end{cases}. \tag{2.72}$$

The kernel is given by

$$[\![\partial_{N'} g_0(\boldsymbol{x}|\boldsymbol{x}')]\!] = [(x_1 - x'_1)\partial_{x'_1}\zeta(\boldsymbol{x}'_\parallel) + (x_2 - x'_2)\partial_{x'_2}\zeta(\boldsymbol{x}'_\parallel) - (\zeta(\boldsymbol{x}_\parallel) - \zeta(\boldsymbol{x}'_\parallel))]\left(\frac{i\frac{\omega}{c}}{R} - \frac{1}{R^2}\right)\frac{e^{i\frac{\omega}{c}}}{R}, \tag{2.73}$$

where the distance between $\boldsymbol{x}$ and $\boldsymbol{x}'$, evaluated at the surface, denoted R, is

$$R = [(x_1 - x'_1)^2 + (x_2 - x'_2)^2 + (\zeta(\boldsymbol{x}_\parallel) - \zeta(\boldsymbol{x}'_\parallel))^2]^{\frac{1}{2}}. \tag{2.74}$$

We replace the integral over the entire x_1x_2-plane with a integration over a finite, square region, $-L/2 \leq x'_1, x'_2 \leq L/2$, much larger than the illuminated area of the surface. The surface is divided into N equal regions of length $\Delta x = L/N$ along the x_1- and x_2-axis, resulting in N^2 square regions of size $(\Delta x)^2$. The centre of the regions are given by

$$\boldsymbol{x}_\parallel(m_1, m_2) = \left(-\frac{L}{2} + \left(m_1 - \frac{1}{2}\right)\Delta x, -\frac{L}{2} + \left(m_2 - \frac{1}{2}\right)\Delta x, 0\right), \quad m_1, m_2 = 1, 2, \ldots N. \tag{2.75}$$

The integral over $\boldsymbol{x}'_\parallel$ can be split into a sum over the regions

$$\int \mathrm{d}^2x'_\parallel \, [\![\partial_{N'} g_0(\boldsymbol{x}|\boldsymbol{x}')]\!]\mathcal{F}(\boldsymbol{x}'_\parallel|\omega) = \sum_{m_1,m_2}^{N} \int_{\Omega(m_1,m_2)} \mathrm{d}^2x'_\parallel \, [\![\partial_{N'} g_0(\boldsymbol{x}|\boldsymbol{x}')]\!]\mathcal{F}(\boldsymbol{x}'_\parallel(m_1, m_2)|\omega), \tag{2.76}$$

where $\Omega(m_1, m_2)$ is the square area around the point $\boldsymbol{x}_\parallel(m_1, m_2)$ of size $(\Delta x)^2$. The field at the surface, $\mathcal{F}$, varies slowly over a short interval, and can be considered constant over $\Omega(m_1, m_2)$, and thus moved out of the integral

$$\int \mathrm{d}^2 x'_\parallel [\![\partial_{N'} g_0(\boldsymbol{x}|\boldsymbol{x}')]\!] \mathcal{F}(\boldsymbol{x}'_\parallel|\omega) = \sum_{m_1,m_2}^{N} \mathcal{F}(\boldsymbol{x}'_\parallel(m_1,m_2)|\omega) \int_{\Omega(m_1,m_2)} \mathrm{d}^2 x'_\parallel [\![\partial_{N'} g_0(\boldsymbol{x}|\boldsymbol{x}')]\!]. \tag{2.77}$$

The integral over the Green's function is then approximated by a sum, giving

$$\int \mathrm{d}^2 x'_\parallel [\![\partial_{N'} g_0(\boldsymbol{x}|\boldsymbol{x}')]\!] \mathcal{F}(\boldsymbol{x}'_\parallel|\omega) \approx (\Delta x)^2 \sum_{m_1,m_2}^{N} [\![\partial_{N'} g_0(\boldsymbol{x}|\boldsymbol{x}')]\!] \mathcal{F}(\boldsymbol{x}'_\parallel(m_1,m_2)|\omega). \tag{2.78}$$

The Cauchy principal value in the integral equation corresponds to excluding the point $\boldsymbol{x}_\parallel = \boldsymbol{x}'_\parallel$ from the sum, according to (2.72),

$$\mathcal{F}(\boldsymbol{x}_\parallel|\omega) = 2\mathcal{F}^{(i)}(\boldsymbol{x}_\parallel|\omega) + \frac{1}{2\pi}(\Delta x)^2 {\sum_{m_1,m_2}^{N}}' [\![\partial_{N'} g_0(\boldsymbol{x}|\boldsymbol{x}')]\!] \mathcal{F}(\boldsymbol{x}'_\parallel(m_1,m_2))|\omega), \tag{2.79}$$

where the prime on the sum denotes that the term $\boldsymbol{x}_\parallel = \boldsymbol{x}'_\parallel$ is excluded.

2.4.6.2 Dirichlet boundary condition

We use the same approach for the Dirichlet boundary condition as for the Neumann boundary condition. We evaluate (2.48) above and below the surface and add the resulting equations. This gives a Fredholm integral equation of the first kind,

$$2\mathcal{F}^{(i)}(\boldsymbol{x}_\parallel|\omega) = \frac{1}{2\pi} \mathrm{P} \int \mathrm{d}^2 x_\parallel [\![g_0(\boldsymbol{x}|\boldsymbol{x}')]\!] \mathcal{N}(\boldsymbol{x}'_\parallel|\omega). \tag{2.80}$$

Here we have used that the singularity of $[\![g_0(\boldsymbol{x}|\boldsymbol{x}')]\!]$ at $\boldsymbol{x} = \boldsymbol{x}'$ is integrable, that is,

$$\int \mathrm{d}^2 x'_\parallel g_0(\boldsymbol{x}|\boldsymbol{x}')\Big|_{\substack{x'_3=\zeta(\boldsymbol{x}'_\parallel) \\ x_3=\zeta(\boldsymbol{x}_\parallel)\pm\eta}} \mathcal{N}(\boldsymbol{x}'_\parallel|\omega) = \int \mathrm{d}^2 x'_\parallel [\![g_0(\boldsymbol{x}|\boldsymbol{x}')]\!] \mathcal{N}(\boldsymbol{x}'_\parallel|\omega). \tag{2.81}$$

A more convenient expression can be obtained by applying ∂_N, Eq. (2.45), on both sides of the equation, above and below the boundary. Combining the resulting equations gives

$$\theta(x_3 - \zeta(\boldsymbol{x}_\parallel))\partial_N \psi(\boldsymbol{x}|\omega) = \partial_N \psi(\boldsymbol{x}|\omega)_{\mathrm{inc}} - \frac{1}{2\pi} \mathrm{P} \int \mathrm{d}^2 x_\parallel \left(\partial_{N'} g_0(\boldsymbol{x}|\boldsymbol{x}')\right)\big|_{x'_3=\zeta(\boldsymbol{x}'_\parallel)} N(\boldsymbol{x}'_\parallel|\omega). \tag{2.82}$$

Evaluating this above and below the surface and adding the resulting equations gives

$$\mathcal{N}(\boldsymbol{x}_\parallel|\omega) = 2\mathcal{N}^{(i)}(\boldsymbol{x}_\parallel|\omega) - \frac{1}{2\pi}\mathrm{P}\int \mathrm{d}^2x_\parallel [\![\partial_N g_0(\boldsymbol{x}|\boldsymbol{x}')]\!]\mathcal{N}(\boldsymbol{x}'_\parallel|\omega) \tag{2.83}$$

where

$$\mathcal{N}^{(i)}(\boldsymbol{x}_\parallel|\omega) = \partial_N \psi(\boldsymbol{x}|\omega)_{\mathrm{inc}}\big|_{x_3=\zeta(\boldsymbol{x}_\parallel)}. \tag{2.84}$$

The kernel is given by

$$\begin{aligned}[\![\partial_{N'} g_0(\boldsymbol{x}|\boldsymbol{x}')]\!] = [&-\partial_{x'_1}\zeta(\boldsymbol{x}'_\parallel)(x_1 - x'_1) - \partial_{x'_2}\zeta(\boldsymbol{x}'_\parallel)(x_2 - x'_2) \\ &+(\zeta(\boldsymbol{x}_\parallel) - \zeta(\boldsymbol{x}'_\parallel))]\left(\frac{i\frac{\omega}{c}}{R} - \frac{1}{R^2}\right)\frac{e^{i\frac{\omega}{c}}}{R},\end{aligned} \tag{2.85}$$

where R is given by Eq. (2.74). Writing Eq. (2.83) as a matrix equation, using the same argument as in Eqs. (2.76) and (2.77), gives

$$\mathcal{N}(\boldsymbol{x}_\parallel|\omega) = 2\mathcal{N}^{(i)}(\boldsymbol{x}_\parallel|\omega) - \frac{1}{2\pi}(\Delta x)^2 {\sum_{m_1,m_2}}' \mathcal{N}(\boldsymbol{x}'_\parallel|\omega)\mathrm{P}\int \mathrm{d}^2x_\parallel [\![\partial_{N'} g_0(\boldsymbol{x}|\boldsymbol{x}')]\!], \tag{2.86}$$

which is similar to the expression in Eq. (2.79) for the Neumann boundary condition. Both these equations can be solved numerically, as we will see in Sec. 3.2.

2.4.7 Kirchhoff approximation

For both the Neumann and Dirichlet boundary condition, we can obtain a first order, single scattering solution to the wave scattering problem by including only the first term on the right hand side of Eqs. (2.79) and (2.86). This gives a fast way of calculating an approximate solution, valid for weakly rough surfaces, called the Kirchhoff approximation.

In the Kirchhoff approximation, Eq. (2.79) inserted into Eq. (2.55) for the Neumann boundary condition gives

$$\begin{aligned}R_N(\boldsymbol{q}_\parallel, \omega) = \frac{-1}{\alpha_0(q_\parallel)}\int \mathrm{d}^2x_\parallel\, \mathcal{F}^{(i)}(\boldsymbol{x}_\parallel|\omega)[\boldsymbol{q}_\parallel \cdot \nabla\zeta(\boldsymbol{x}_\parallel) - \alpha_0(q_\parallel)] \\ \cdot e^{-i\boldsymbol{q}_\parallel \cdot \boldsymbol{x}_\parallel - i\alpha_0(q_\parallel)x_3}.\end{aligned} \tag{2.87}$$

Using the definition of the incident field, Eq. (2.71),

$$\begin{aligned}= \frac{-1}{\alpha_0(q_\parallel)}\int \mathrm{d}^2x_\parallel \left[\frac{w^2}{2\pi}\int_{u_\parallel < \frac{\omega}{c}} \mathrm{d}^2u_\parallel e^{i\boldsymbol{u}_\parallel \cdot \boldsymbol{x}_\parallel - i\alpha_0(u_\parallel)x_3} e^{-\frac{w^2}{2}(\boldsymbol{u}_\parallel - \boldsymbol{k}_\parallel)^2}\right]\Bigg|_{x_3=\zeta(\boldsymbol{x}_\parallel)} \\ \cdot [\boldsymbol{q}_\parallel \cdot \nabla\zeta(\boldsymbol{x}_\parallel) - \alpha_0(q_\parallel)]e^{-i\boldsymbol{q}_\parallel \cdot \boldsymbol{x}_\parallel - i\alpha_0(q_\parallel)x_3}\end{aligned} \tag{2.88}$$

Similarly for the Dirichlet boundary condition, inserting Eq. (2.51) into Eq. (2.86) and using the definition of the incident field, Eq. (2.84), gives

$$\begin{aligned} R_D(\boldsymbol{q}_\parallel,\omega) =& \frac{-i}{\alpha_0(q_\parallel)} \int \mathrm{d}^2 x_\parallel \left[\partial_N \frac{w^2}{2\pi} \int\limits_{u_\parallel < \frac{\omega}{c}} \mathrm{d}^2 u_\parallel e^{i\boldsymbol{u}_\parallel \cdot \boldsymbol{x}_\parallel - i\alpha_0(u_\parallel)x_3} e^{-\frac{w^2}{2}(\boldsymbol{u}_\parallel - \boldsymbol{k}_\parallel)^2} \right] \Bigg|_{x_3=\zeta(\boldsymbol{x}_\parallel)} \\ & \cdot e^{-i\boldsymbol{q}_\parallel \cdot \boldsymbol{x}_\parallel - i\alpha_0(q_\parallel)x_3} \\ =& \frac{-1}{\alpha_0(q_\parallel)} \int \mathrm{d}^2 x_\parallel \left[\frac{w^2}{2\pi} \int\limits_{u_\parallel < \frac{\omega}{c}} \mathrm{d}^2 u_\parallel [\boldsymbol{u}_\parallel \cdot \nabla\zeta(\boldsymbol{x}_\parallel) + \alpha_0(u_\parallel)] \right. \\ & \left. \cdot e^{i\boldsymbol{u}_\parallel \cdot \boldsymbol{x}_\parallel - i\alpha_0(u_\parallel)x_3} e^{-\frac{w^2}{2}(\boldsymbol{u}_\parallel - \boldsymbol{k}_\parallel)^2} \right] \Bigg|_{x_3=\zeta(\boldsymbol{x}_\parallel)} e^{-i\boldsymbol{q}_\parallel \cdot \boldsymbol{x}_\parallel - i\alpha_0(q_\parallel)x_3}. \end{aligned} \tag{2.89}$$

The only difference between Eqs. (2.88) and (2.89) is that the $\boldsymbol{q}_\parallel \cdot \nabla\zeta(\boldsymbol{x}_\parallel) - \alpha_0(q_\parallel)$ factor works on the upward scattered vector $\boldsymbol{q}$ for the Neumann case and the downward directed incident beam component $\boldsymbol{u}$ for the Dirichlet case, and the sign in front of $\alpha_0(q_\parallel)$. For specular scattering, the difference between $\boldsymbol{q}$ and $\boldsymbol{u}$ is just a sign change for the third component, giving that $R_N = R_D$ in the Kirchhoff approximation. The equivalent expressions in the Kirchhoff approximation corresponds to single scattering where the scattered intensity only depends on local slope, as the Fresnel coefficients for a non-absorbing, non-transparent medium gives total reflection [20].

3 Method

The computational methods used to calculate incident beam and set up and solve the system matrix is introduced here. Once a solution to the system matrix is found, the mean differential reflection coefficient is calculated from the surface field. The method used for generating the random surfaces are also presented, along with the approach taken to parallelise the implementation of the matrix element generation and scattered field calculation.

3.1 Incident wave

The incident Gaussian wave is created by summing a set of plane waves modulated by a Gaussian envelope. This gives a Gaussian incident beam centred around the angle of incidence, with the desired half width. The integral for the incident power, Eq. (2.65), containing a zero order Bessel function of the first kind, must be evaluated to compare the incident and scattered power. The integral is evaluated by numerical integration, either by the midpoint method or by using the QUADPACK routine QAGS [7].

As the width of the beam increases, the Gaussian beam approaches a plane wave. For a plane incident wave, the incident power is known to be proportional to $L_1 L_2 \alpha_0(k_\parallel)$ [10]. If we expand $\alpha_0(q_\parallel)$ in a Taylor series for $\boldsymbol{q}_\parallel$ around $\boldsymbol{k}_\parallel$ up to first order in $(\boldsymbol{q}_\parallel - \boldsymbol{k}_\parallel)$, we obtain

$$\begin{aligned}\psi(\boldsymbol{x}|\omega)_{\text{inc}} \approx & \frac{w^2}{2\pi} \exp\left[i\boldsymbol{k}_\parallel \cdot \boldsymbol{x}_\parallel - i\alpha_0(k_\parallel)x_3\right] \\ & \cdot \int \mathrm{d}^2 u_\parallel \exp\left[i\left(\boldsymbol{x}_\parallel + x_3 \frac{\boldsymbol{k}_\parallel}{\alpha_0(k_\parallel)}\right) \cdot \boldsymbol{u}_\parallel - \frac{w^2}{2}\boldsymbol{u}_\parallel^2\right] \\ = & \exp\left[i\boldsymbol{k}_\parallel \cdot \boldsymbol{x}_\parallel - i\alpha_0(k_\parallel)x_3\right] \exp\left[-\frac{1}{2w^2}\left(\boldsymbol{x}_\parallel + x_3 \frac{\boldsymbol{k}_\parallel}{\alpha_0(k_\parallel)}\right)^2\right]. \end{aligned} \tag{3.1}$$

Inserting this into Eq. (2.65) gives

$$P_{\text{inc}} = \frac{\hbar}{m}\alpha_0(k_\parallel) \exp\left[-\frac{1}{w^2}\left(\boldsymbol{x}_\parallel + x_3 \frac{\boldsymbol{x}_\parallel}{\alpha_0(k_\parallel)}\right)^2\right], \tag{3.2}$$

proportional to $\frac{\hbar}{m}\alpha_0(k_\parallel)$ times the area of the illuminated surface, which is $L_1 L_2$ for a plane wave.

Increasing the polar angle of incidence to large angles gives some additional problems, as the incident beam illuminates the edges of the surface. This can be avoided by scaling

the width of the incident beam with the incident polar angle, such that the illuminated spot on the surface stays circular and within the finite surface for all angles of incidence. Depending on boundary condition, the only needed part of the incident field is either the field at the surface or the normal derivative of the field at the surface.

3.2 System matrix

The integral equations, Eqs. (2.52) and (2.48) must be discretised in order to obtain the matrix equation. The extended midpoint method[8],

$$\int_{x_0}^{x_{N-1}} f(x) = h\left[f_{1/2} + f_{3/2} + f_{5/2} + \cdots + f_{N-5/2} + f_{N-3/2}\right] + O\left(\frac{1}{N^2}\right), \quad (3.3)$$

where the limits of integration are located halfway between tabulated abscissas, is generalised to two-dimensions and used when discretising the integral equations.

When the integral is rewritten in matrix form as in Eqs. (2.79) and (2.86), the scattered field at the surface can be obtained by solving the matrix system. Reordering the elements gives, in the Neumann boundary condition case

$$\sum_{m_1,m_2}^{N} \left(\delta(\boldsymbol{x}'_\parallel - \boldsymbol{x}_\parallel) - \frac{1}{2\pi}(\Delta x)^2 [\![\partial_{N'} g_0(\boldsymbol{x}|\boldsymbol{x}')]\!]\right) \mathcal{F}(\boldsymbol{x}'_\parallel(m_1,m_2)|\omega) = 2\mathcal{F}^{(i)}(\boldsymbol{x}_\parallel|\omega), \quad (3.4)$$

where the delta function comes from the left hand side of Eq. (2.79).

The Green's function in Eq. (2.39) must be discretised in the surface grid. This is done by evaluating the Green's function in the x_1x_2-grid. The principal value is handled by setting the terms where $\boldsymbol{x} = \boldsymbol{x}'$ to zero. Each relation between two surface point is described by a single, complex number in the system matrix, compared to 8 complex numbers for the perfect conductor polarised wave.

Using Eq. (3.4), we get the integral equations is on a form of a linear system $\mathrm{A}\boldsymbol{x} = \boldsymbol{b}$ where A is a dense, complex system matrix. The right hand side, $\boldsymbol{b}$, describes the incident field and the unknown vector $\boldsymbol{x}$ consists of the surface field, $\mathcal{F}^{(i)}(\boldsymbol{x}_\parallel|\omega)$ or $\mathcal{N}^{(i)}(\boldsymbol{x}_\parallel|\omega)$, depending on the surface condition. Discretising the surface function $x_3 = \zeta(\boldsymbol{x}_\parallel)$ into a $N \times N$ point grid gives N^2 unknowns in the vector $\boldsymbol{x}$, one unknown for each point in the grid. The full system matrix then consists of N^4 elements.

Solving this large matrix system is rather time consuming. As the system matrix is dense and asymmetric, there is a limited number of effective solution methods. Decomposition of the system matrix using LU-decomposition is a possibility that gives the advantage of being able to quickly compute the resulting surface field for a given surface for many different incident beams. The major disadvantage for this method is the $O(n^3)$ complexity for an n column square matrix, which can be reduced to $O(n^{2.807})$ using the Strassen algorithm for matrix multiplication[15]. Alternatively one can use an iterative matrix solver.

The resulting expression for Neumann boundary condition depends only on the value of the field at the surface. Using the Dirichlet boundary condition, the equation only depends on the normal derivative of the field at the surface. For both boundary conditions, the resulting system matrix is the same, except from being written in terms of the field or in terms of the normal derivative of the field and from taking the normal derivative of the incident or the scattered wave vector. Using that the system matrix only depends on either the field or the normal derivative of the field, the same approach can be used for both boundary conditions, expressing the field or the normal derivative of the field as a general field component at each surface point.

3.3 Linear system solver

The field at the surface for the Neumann problem is calculated from Eq. (2.79). Similarly the normal derivative of the field for the Dirichlet problem is calculated from Eq. (2.86). The resulting matrix system is a large, dense, non-symmetric matrix. Solving the matrix system is numerically heavy, as efficient solution methods that exist for sparse matrices and matrices with symmetries can not be used.

Using an iterative solver, convergence is reached for most surfaces in less than 20 iterations, less for less rough surfaces. Using an efficient iterative method such as BiCGStab(ℓ), based on BiCGStab [19], gives a good trade-off between memory usage and computational time. Compared to alternative, iterative methods for solving dense matrix systems, such as Bi-CG, CGS and GMRES, BiCGStab performs well. It requires $0.75(\ell+3)$ matrix-vector-products per iteration, converges fast compared to alternative methods and is stable in most cases, although it is not guaranteed. Further details on BiCGStab(ℓ) compared to alternative iterative methods can be found in Ref. [13].

Using a preconditioner can improve the rate of convergence, but in contrast to algorithms such as Bi-CG and GCR, there is no variant of the preconditioned BiCGStab(ℓ) that generates both the real residual and the approximation we are interested in without demanding additional computational work or storage. The possible preconditioners are $H_0 A = H_0 \boldsymbol{b}$ and $A H_0 \boldsymbol{y} = \boldsymbol{b}$ with $\boldsymbol{x} = H_0 \boldsymbol{y}$ where H_0 is the preconditioning matrix.

As a side note, if the scattered intensity is to be calculated for a large number of incident beams, it is more effective to calculate the inverse of the system matrix, as this only has to be done once for a given surface. Each calculation for a new incident beam is then only a matter of multiplying the inverse matrix by the right hand side for each incident beam.

3.4 Surface field

Evaluating the incident field at the surface and calculating the scattered field at the surface gives a single value at each surface point. This is the equivalent of the surface current for polarised, electromagnetic waves. The main difference lies in that the scalar wave only has one component, compared to two independent components for each of

the two surface current vectors, for a total of four for the perfect conductor, and six components for the general metal. The scalar wave does not contain the polarisation information seen in the electromagnetic simulation.

3.5 Mean differential reflection coefficient

Obtaining the reflection coefficient requires different approaches for the two boundary conditions, Eqs. (2.55) and (2.51). In both cases, we integrate the surface field, or the normal derivative of the field for the Dirichlet boundary condition, over the surface, obtaining the reflection coefficient. The integral over $x_{\parallel}$ is done as a sum over the finite region, $-L/2 < x_1, x_2 < L/2$.

The mean differential reflection coefficient (MDRC), $\left\langle \frac{\partial R}{\partial \Omega_s} \right\rangle$, is defined as the fraction of the total incident power scattered into a small solid angle $d\Omega_s$ about the scattering direction (θ_s, ϕ_s). Using the MDRC, one finds a physically measurable size from the simulations,

$$\left\langle \frac{\partial R}{\partial \Omega_s} \right\rangle = \frac{p_{\mathrm{sc}(\theta_\mathrm{s},\phi_\mathrm{s})}}{P_{\mathrm{inc}}}, \tag{3.5}$$

where $p_{\mathrm{sc}(\theta_\mathrm{s},\phi_\mathrm{s})}$ is the power scattered into (θ_s, ϕ_s), Eq. (2.64), and P_{inc} defined in Eq. (2.66).

The factor $\left\langle |R(q|k)|^2 \right\rangle$ in Eq. (2.67) when it is averaged over an ensemble of surface realisations, can be rewritten as

$$\left\langle |R(q|k)|^2 \right\rangle = \left\langle |R(q|k)|^2 \right\rangle - |\left\langle R(q|k) \right\rangle|^2 + |\left\langle R(q|k) \right\rangle|^2. \tag{3.6}$$

The last term describes the coherently scattered wave and the first two terms incoherently part of the scattered wave. This makes it possible to find the coherent and incoherent component from numerical simulations, where the coherent and incoherent component cannot be calculated separately.

After having calculated the amplitudes of the scattered field from the surface field, the mean differential reflectance coefficient can be found from the reflectance amplitude, R and $|R|^2$. Taking the mean of these sizes over each surface realisation we obtain $\langle R \rangle$ and $\langle |R|^2 \rangle$. The coherent and incoherent component can then be obtained from equation (3.5), giving the equations

$$\left\langle \frac{\partial R}{\partial \Omega_s} \right\rangle_{\mathrm{coh}} = |\langle R \rangle|^2, \tag{3.7}$$

$$\left\langle \frac{\partial R}{\partial \Omega_s} \right\rangle_{\mathrm{incoh}} \approx \langle |R|^2 \rangle - |\langle R \rangle|^2, \tag{3.8}$$

with a prefactor calculated from the total incident power and the parameters of the media.

3.6 Energy conservation

When a surface is illuminated by a source, the incident beam will be split into a reflected, a transmitted and an absorbed part. Summing over these components, the total energy should be equal to the initial energy of the incident beam. If there is no transmission and no absorption, the total reflected energy should be equal to the incident energy. Defining the quantity

$$\mathcal{U}(\theta_0, \phi_0) = \int \mathrm{d}\Omega_s \left\langle \frac{\partial R}{\partial \Omega_s} \right\rangle, \tag{3.9}$$

gives an expression for the fraction of the incident power that is scattered. If the lower medium is non-absorbing, the total incident energy should be conserved and either reflected off or transmitted trough the surface. For a hard surface there will be no absorption, and all incident power flux will be converted into reflected power flux,

$$\mathcal{U}(\theta_0, \phi_0) = 1. \tag{3.10}$$

This is equivalent to conservation of energy, and gives a simple and necessary, but not sufficient, measure of the quality of the simulation.

3.7 Parallelisation

The numerically heavy parts are solving the system matrix, generating the system matrix and calculating the reflection coefficients, as seen from Tab. 3.1. The system matrix generation is independent for each matrix element, making it trivially parallelisable. The scattering coefficient can also be calculated independently for each direction, once the surface field is known. The matrix set-up can be done without access to the full matrix, whereas the surface field calculation needs read access to the entire matrix, but only does local writing of results.

Parallelisation of the system matrix solving requires more work. Each BiCGStab operation requires three matrix-vector multiplications. The multiplication is done efficiently using BLAS[2]. Parallelisation requires either a full parallel implementation of the BiCGStab-routine, or a multithreaded BLAS-library that can be used in the matrix-vector products.

The limiting factor in rigorous simulation of large systems is the memory requirements when solving the matrix system. Thus it is important to keep the number of elements on each node as low as possible. The memory requirement to hold the system matrix scales as N^4 for a $N \times N$ point surface. An efficient approach for distributed memory systems depends on a good distributed iterative matrix solver. Keeping the BiCGStab used in the single threaded approach and looking for a efficient parallel implementation of the iterative solver, is a starting point, as the BiCGStab solver has shown good performance in the single threaded implementation. The solver natively requires communication between the nodes at each matrix product. An efficient implementation

requires rearranging the elements of the system matrix such that inter-node communication before and after each vector-matrix-product in each BiCGStab iteration is reduced. This approach requires a larger change in the code relative to the single threaded version.

As the solution is averaged over a large number of surface realisations, large scale parallelisation over different surface realisations might be used. Available memory is the limiting factor for solving larger systems, so the parallelisation reduces the size of the system that can be simulated with a factor inversely proportional to the number of parallel instances, when running on systems with shared memory and multiple processors.

Function	time used (%)
Calculate reflectance amplitude	47%
BiCGStab	28%
System matrix set-up	25%

Table 3.1: Amount of time used in the various parts of the simulation, obtained from profiling a simulation of 100 samples with 3 incident angles using a 100×100 point surface grid discretisation and a 101×101 point momentum grid for the scattered wave. Using a $\delta = 0.5\lambda$, $a = 2.0\lambda$ surface, the iterative solver converges after about 35 iterations. Only the top three functions are listed, the remaining functions account for less than 1%. The system matrix is set up once per surface, the iterative solver is run once for each incident angle for each surface and the reflectance amplitude is run once for each surface and iterates over the incident angles.

3.8 Surface generation

The correlated surfaces is generated by the Fourier filtering method. First a set of Gaussian random numbers with unity standard deviation is generated, one for each surface point. Then a two-dimensional Fourier transform is performed on the grid of random numbers. We then filter the Fourier transformed numbers with the square root of the wanted power spectrum, $\sqrt{g(\boldsymbol{k})}$. To obtain the wanted standard deviation of the resulting surface, all points on the surface is scaled with the wanted standard deviation. Finally, we take the inverse Fourier transform to obtain the surface with the desired correlation length and standard deviation.

3.8.1 Anisotropic surface

Introducing an anisotropy requires a power spectral density that have different correlation lengths along the x_1- and x_2-direction,

$$g(\boldsymbol{k}) = \pi a_1 a_2 \exp\left[-\frac{k_1^2 a_1^2}{4} - \frac{k_2^2 a_2^2}{4}\right], \tag{3.11}$$

the Fourier transform of the anisotropic correlation function, Eq. (2.7). Except from the new power spectrum used in the filtering part, the method for generating the surfaces is the same as for the isotropic surfaces.

3.8.2 Self-affine surface

The self-affine surfaces can be generated in a similar way as the correlated surfaces. Fourier filtering with the power spectrum of the self-affine surface, dependent on the Hurst exponent, H, Eq. (2.19), the random numbers can be filtered into a self-affine correlation between adjacent surface points. The second parameter describing the self-affine surface, the topothesy, has to be calculated after the surface is transformed back to real space. The topothesy is calculated by Eq. (2.12). Once the topothesy of the generated surface is obtained, the surface is scaled with a factor $(\frac{\ell_0}{\ell})^{1-H}$ where ℓ is the calculated topothesy and ℓ_0 is the wanted topothesy.

In obtaining the topothesy of the surface, we use a distance between surface points of $n = N/4$. The calculated topothesy is averaged over the surface in two dimensions, and averaged over a scan with Δx along x_1 and along x_2. The resulting surfaces have been plotted and compared for different parameters using the same random numbers. The topothesy of the generated surfaces have also been calculated for a range of n, giving similar values for the topothesy measurement for $n \in [2, N/2]$.

3.9 Diffuse expansion

The MDRC for a plane incident wave scattered from a self-affine surface in the Kirchhoff approximation is [14]

$$\begin{aligned}\left\langle \frac{\partial R}{\partial \Omega_s} \right\rangle =& \frac{1}{2\pi \cos\theta_0} \frac{[(\omega/c)^2 + \alpha_0(q_\parallel)\alpha_0(k_\parallel) - \boldsymbol{q}_\parallel \cdot \boldsymbol{k}_\parallel]^2}{[\alpha_0(q_\parallel) + \alpha_0(k_\parallel)]^2} \\ & \cdot \int_0^\infty \mathrm{d}v_\parallel \; v_\parallel \exp[-\frac{1}{2}(\ell^{1-H} v_\parallel^H)^2 (\alpha_0(q_\parallel) + \alpha_0(k_\parallel))^2] J_0(Q_\parallel v_\parallel).\end{aligned} \tag{3.12}$$

An expansion for small parameters can be obtained [14]. Rewriting Eq. (3.12) using

$$u_{\parallel} = \ell^{\frac{1}{1-H}} \left(\frac{\alpha_0(q_{\parallel}) + \alpha(k_{\parallel})}{\sqrt{2}} \right)^{1/H} v_{\parallel} \equiv A v_{\parallel}, \tag{3.13}$$

$$\mathrm{d}v_{\parallel} = \frac{\mathrm{d}u_{\parallel}}{A}, \tag{3.14}$$

$$C \equiv \frac{1}{2\pi \cos\theta_0} \frac{[(\omega/c)^2 + \alpha_0(q_{\parallel})\alpha_0(k_{\parallel}) - \boldsymbol{q}_{\parallel} \cdot \boldsymbol{k}_{\parallel}]^2}{[\alpha_0(q_{\parallel}) + \alpha_0(k_{\parallel})]^2}, \tag{3.15}$$

which gives

$$\left\langle \frac{\partial R}{\partial \Omega_s} \right\rangle = C \int_0^{\infty} \mathrm{d}u_{\parallel} \, \frac{u_{\parallel}}{A^2} \exp[-|u_{\parallel}|^{2H}] J_0(\frac{Q_{\parallel}}{A} u_{\parallel}), \tag{3.16}$$

where the integral essentially is the Hankel transform. Applying the Taylor series expansion to the Bessel function and doing the substitution $t = u_{\parallel}^{2H}$ and $\alpha = 2H$ gives

$$\left\langle \frac{\partial R}{\partial \Omega_s} \right\rangle \approx \frac{C}{\alpha A^2} \int_0^{\infty} \mathrm{d}t \; e^{-t} e^{(2/\alpha - 1)} - \frac{C Q_{\parallel}^2}{4\alpha A^4} \int_0^{\infty} \mathrm{d}t \; e^{-t} e^{(4/\alpha - 1)}. \tag{3.17}$$

Identifying the gamma function and writing this out, one obtains the specular expansion,

$$\begin{aligned} \left\langle \frac{\partial R}{\partial \Omega_s} \right\rangle \approx & \frac{[(\omega/c)^2 + \alpha_0(q_{\parallel})\alpha_0(k_{\parallel}) - \boldsymbol{q}_{\parallel} \cdot \boldsymbol{k}_{\parallel}]^2}{8\pi H \cos\theta_0 [(\alpha_0(q_{\parallel}) + \alpha_0(k_{\parallel}))/\sqrt{2}]^{2/H+2} \ell^{2/H-2}} \\ & \cdot \left(\Gamma(1/H) - \frac{\Gamma(2/H) Q_{\parallel}^2}{4} \left[\frac{\alpha_0(q_{\parallel})\alpha_0(k_{\parallel})}{\sqrt{2}} \right]^{-2/H} \right) \ell^{-(2/H-2)}. \end{aligned} \tag{3.18}$$

We seek a way to obtain an approximation for the diffuse component of the scattered light, similar to the one obtained for one-dimensional surfaces in Ref. [11], which should be a good approximation far away from the specular direction. We use the large parameter expansion of the zero order Bessel function of the first kind, valid for $x \gg |1/4|$ [1],

$$J_0(x) \approx \sqrt{\frac{2}{\pi x}} \cos(x - \pi/4). \tag{3.19}$$

With this expansion, Eq. (3.16) can be written as

$$\left\langle \frac{\partial R}{\partial \Omega_s} \right\rangle \approx D \int_0^{\infty} \mathrm{d}u_{\parallel} \sqrt{u_{\parallel}} \exp\left[-|u_{\parallel}|^{2H}\right] \cos\left(\frac{Q_{\parallel} u_{\parallel}}{A} - \frac{\pi}{4} \right), \tag{3.20}$$

where

$$D = C \sqrt{\frac{2}{A\pi Q_{\parallel}}}. \tag{3.21}$$

This corresponds to the contribution to the total MDRC coming from scattering outside the specular direction. In the case where $H = 1/2$, corresponding to a surface generated by a random walk, Eq. (3.20) reduces to a simpler form,

$$\left\langle \frac{\partial R}{\partial \Omega_s} \right\rangle \approx D \int_0^\infty \mathrm{d}u_\parallel \sqrt{u_\parallel} \exp[-u_\parallel] \cos\left(\frac{Q_\parallel u_\parallel}{A} - \frac{\pi}{4} \right), \tag{3.22}$$

which is divergent, for all values of $Q_\parallel$, and contains upper incomplete gamma functions on the form

$$\Gamma(\frac{3}{2}, x) = \int_x^\infty \mathrm{d}t \; t^{1/2} e^{-3/2}, \tag{3.23}$$

with complex x when integrated from 0 to $v < \infty$. This does not give any additional insight on the diffuse scattering.

4 Results and discussion

Simulations have been performed for scalar waves scattered from Gaussian correlated and self-affine surfaces, using various surface parameters, boundary conditions and incident beams. The incident beam is described by a beam width, w, polar and azimuthal angle of incidence, θ_0 and ϕ_0. The wavelength of the incident beam and the parameters for each medium are also required to perform the simulation. The wavelength is held at 1μm.

The media considered is a non-dispersive medium in the upper region and a non-penetrable medium in the lower region, separated by a surface described by a hard wall or free surface boundary condition. The boundary condition does not allow for waves to propagate on the surface or in the lower medium. However, multiple scattering effects can give waves propagating along the surface, scattered multiple times by the surface roughness before they are scattered back upwards. Thus the size of the surface have to be large enough that multiple scattered beams travelling along the surface do not give a significant contribution at the edge of the surface.

The linear size of the sample is denoted L, limited to $L = 16\lambda$ for rigorous simulations, due to the memory requirements. The surface is discretised with discretisation length $\Delta x = \lambda/7$, onto a $N \times N$-point grid. Decreasing the discretisation length further gives no observable increase in simulation quality. Increasing the beam width increases the incident intensity at the edges of the surface. To make sure that edge effects are insignificant, the half width of the Gaussian beam is limited to $w = L/4$.

The resulting angular distribution of the mean differential reflection coefficient is discretised onto a two dimensional grid of wave vectors, giving a $N_q \times N_q$ element grid. The wave vectors are normalised with ω/c, giving $q_i/(\omega/c) \in [-1, 1]$, $(i = 1, 2)$. The polar angle of incidence is held at $\theta_0 \leq 40°$.

4.1 Gaussian correlated surfaces

We start by looking at correlated surfaces with a Gaussian correlation function and a Gaussian height-distribution, similar to the surfaces used in Ref. [10]. The surface generation requires three parameters for the surface: surface roughness, correlation length and anisotropy ratio. We will study the effect on the scattering pattern from changing each parameter separately.

4.1.1 Boundary condition

The boundary condition chosen for the surface determines how the wave behaves at the surface, either by having zero pressure or zero normal velocity at the surface, as described in Sec. 2.4.1. The scattered intensity behaves similarly for both boundary conditions for a less rough surfaces, Fig. 4.1(a), $\delta = 0.1\lambda$ and correlation length $a = 2\lambda$, as the main contribution comes from single scattering. In that case, as the Kirchhoff approximation is valid, the boundary conditions reduces to the same result, as seen in Sec. 2.4.7, and almost all scattered intensity goes in the forward direction.

As the roughness is increased, Fig. 4.1(c), the contribution from multiple scattering increases, and the difference between the two boundary conditions increases. For $\delta = 0.5\lambda$, the two boundary conditions gives a different shape around the specular direction. Increasing the roughness further to $\delta = 1.0\lambda$, Fig. 4.1(e), gives clear enhanced backscattering, where the two boundary conditions behave similarly. In the low roughness case and the high roughness case the scattered beam goes in either the specular direction or in the backscattering direction, thus being relatively unaffected by switching boundary condition from Neumann to Dirichlet. However, in the middle domain, the scattered intensity is distributed into a diffuse cloud, where the scattering direction is very different from the incident direction.

We speculate that the difference between the boundary conditions, Figs. 4.1(c) and 4.1(d) is caused by a local slope, s, just low enough that multiple scattering only gives a low contribution, giving mainly single scattering, but rough enough that much is scattered away from the specular direction. Using the hard wall boundary condition, this will result in a diffuse peak around the specular direction, however for the free surface, the surfaces ability to move results in a more intense peak at a higher scattering angle than the incident angle, $\theta_s > \theta_0$.

In the following simulations we limit ourselves to either the Dirichlet or Neumann boundary condition, as the observed difference between the two boundary conditions is negligible. Where the results for the two boundary condition differ, such as for rough, anisotropic surfaces, results for both the Neumann and the Dirichlet boundary condition are given.

4.1.2 Varying surface roughness

The surface roughness is one of the important factors in determining how the scattering pattern behaves. It affects the amount of the incident beam that will be scattered in the specular direction and how much will scatter in other directions. It also affects how much of the incident beam will be scattered multiple times and thus the amount of multiple scattering effects.

Increasing the surface roughness moves the main scattered contribution from the specular direction to the backscattering direction, Fig. 4.2, caused by enhanced backscattering. At RMS-roughness $\delta = 0.1\lambda$, and correlation length $a = 2\lambda$, the scattering is mainly in the forward direction. As the roughness is increased, the forward scattering is reduced, and the forward scattering peak grows wider and moves to larger scattering

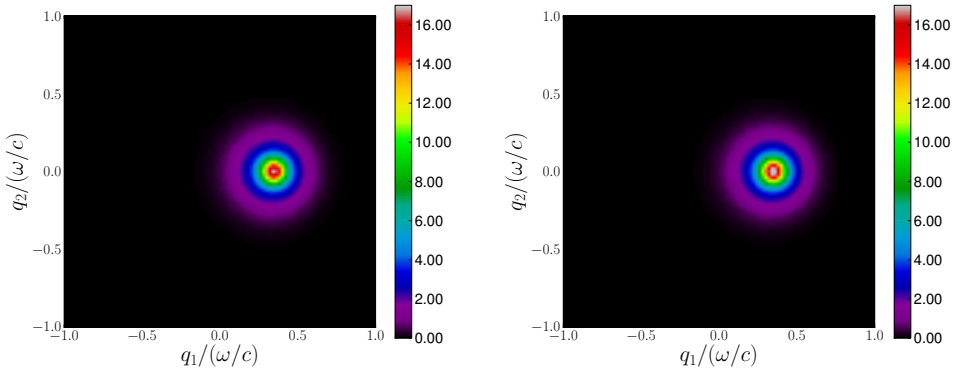

(a) $\delta = 0.1\lambda$, Neumann BC

(b) $\delta = 0.1\lambda$, Dirichlet BC

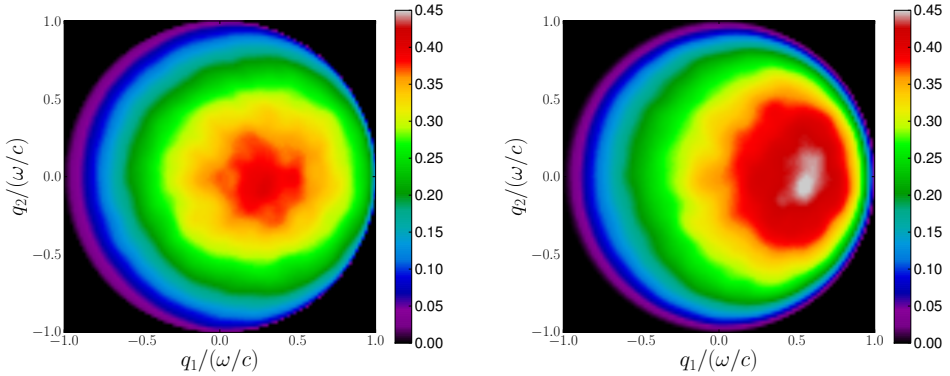

(c) $\delta = 0.5\lambda$, Neumann BC

(d) $\delta = 0.5\lambda$, Dirichlet BC

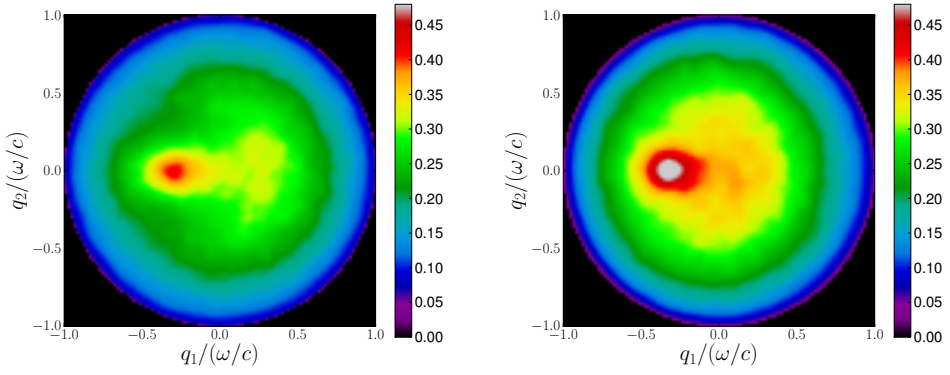

(e) $\delta = 1.0\lambda$, Neumann BC

(f) $\delta = 1.0\lambda$, Dirichlet BC

Figure 4.1: MDRC of a scalar wave scattered from a quadratic, $L = 16\lambda$ isotropic surface, with correlation length $a = 2.0\lambda$, using both the Neumann and Dirichlet boundary conditions for a range of surfaces with different roughness, $\delta \in [0.1\lambda, 1.0\lambda]$. The results is averaged over $N_s = 3500$ samples. The incident beam is a $w = 4\lambda$ wide Gaussian beam with polar and azimuthal angle of incidence $\theta_0 = 20°$ and $\phi_s = 0°$, respectively.

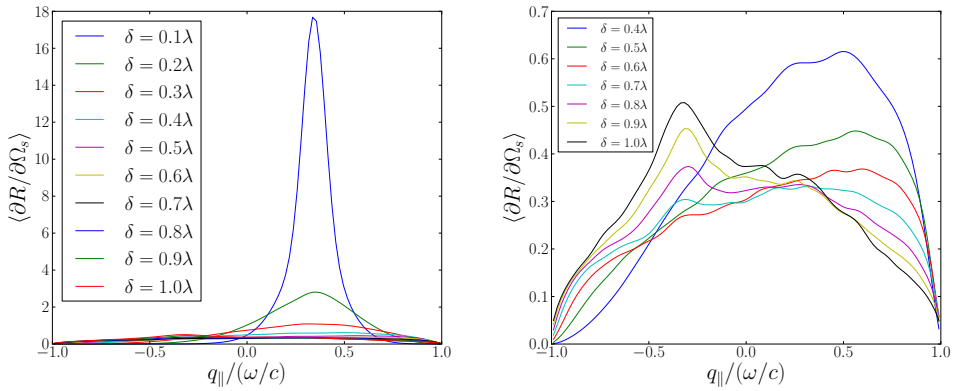

(a) Low δ (b) High δ

Figure 4.2: A cut of the scattering intensity in the plane of incidence. We use a set of surface RMS-roughness in the range (a) $\delta \in [0.1\lambda, 1.0\lambda]$ and (b) $\delta \in [0.4\lambda, 1.0\lambda]$. The correlation length is held constant at $a = 2\lambda$. The isotropic, quadratic, $L = 16\lambda$ surface is described by a Dirichlet boundary condition. The incident beam is a $w = 4\lambda$ wide Gaussian beam with polar angle of incidence $\theta_0 = 20°$. The results have been averaged over $N_s = 4000$ samples.

angles. At $\delta = 0.7\lambda$ the forward and backward scattering is almost equal, with peaks in the forward and backward direction. The forward peak is still at a larger polar scattering angle than the incident beam, $\theta_s > \theta_0$. Increasing the roughness further to $\delta = 0.8\lambda$ and beyond, gives a clear enhanced backscattering peak. The enhanced backscattering comes from double scattering processes, where there are two interactions with the surface before it is scattered away from the surface, giving a larger contribution for rough surfaces as a larger amount of incident paths will result in scattered, downward directed and weakly upward directed waves that will interact with the surface again before they are scattered back up.

Changing the surface roughness while keeping the correlation length constant gives a smooth change from purely specular scattering to diffuse scattering to enhanced backscattering as the surface roughness is increased.

4.1.3 Varying correlation length

As the correlation length is decreased, the coupling between nearby surface points is decreased, resulting in larger local variations, and thus a larger local slope and a larger amount of scattering out of the specular direction.

At larger correlation lengths, Fig. 4.3, $a = 3.0\lambda$, with RMS-roughness $\delta = 0.5\lambda$, most of the scattered intensity goes in the forward direction. Reducing the correlation length, and thus increasing the local slope, the forward scattering is reduced as the scattering

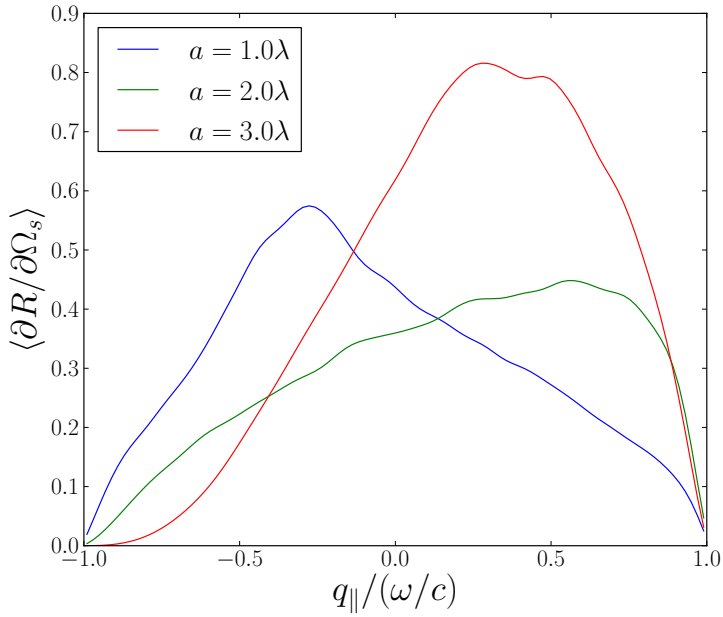

Figure 4.3: A cut of the MDRC in the in the plane of incidence. We use a set of correlation lengths in the range $a \in [1.0\lambda, 3.0\lambda]$ for the surfaces. The roughness held constant at $\delta = 0.5\lambda$ and the surface is isotropic and quadratic with length $L = 16\lambda$. The surface is described by a Dirichlet boundary condition. The Gaussian incident beam has a half width $w = 4\lambda$ and polar angle of incidence $\theta_0 = 20°$. The results have been averaged over $N_s = 3000$ samples.

pattern forms a diffuse, forward peak. The forward peak is also shifted to larger polar scattering angles, larger than the incident angle, $\theta_s > \theta_0$. Reducing the correlation length further gives a clear peak in the backward direction, enhanced backscattering, and no discernible peak in the forward direction.

Changing the correlation length is to a degree similar to changing the inverse surface roughness, as the surface roughness and correlation length couple into a mean slope, giving similar behaviour for low mean slope surfaces. The tendency for the forward peak to move to larger polar scattering angles as the mean slope increases, previously seen when increasing the RMS-roughness, is found here as well, when using the Dirichlet boundary condition.

4.1.4 Varying anisotropy ratio

When we introduce an anisotropy in the surface, the scattered intensity distribution will depend on the azimuthal angle of incidence, ϕ_0, as the alignment between the major and minor correlation axis and the plane of incidence changes. The symmetry

of the scattering pattern around the plane of incidence, seen for isotropic surfaces, is no longer preserved.

For a less rough, $\delta = 0.1\lambda$, $a_1 = 2\lambda$, surface with anisotropy ratio $r = 2.0$, Fig. 4.4(a,c,e), we observe an elliptic peak in the specular direction. As the azimuthal angle of incidence changes, the shape of the peak stays unchanged, stretched out along the minor correlation axis, as the peak moves from $\phi_s = 0°$ to $\phi_s = 90°$, while the azimuthal angle of incidence moves from $\phi_0 = 0°$ to $\phi_0 = 90°$ For a rougher surface, $\delta = 0.5\lambda$, Fig. 4.4(b,d,f), the scattering pattern is stretched out compared to the less rough, $\delta = 0.1\lambda$ surface. The scattering pattern retains the same elliptic shape as for $\delta = 0.1\lambda$, but with a larger, diffuse shape.

As the simulation is done using the Dirichlet boundary condition, we observe the same effect as in Sec. 4.1.1, the forward peak lies at $\theta_s > \theta_0$ for $\phi_0 = 0°$ and $\phi_0 = 45°$. The forward peak moves to $\theta_s = \theta_0$ as the incident beam moves to $\phi_0 = 90°$, plane of incidence along the major correlation axis. We speculate that this is caused by the increasing correlation length along the plane of incidence, giving a smoother surface as seen from the incident direction, and thus less steep slope and behaviour more like for the hard wall, Neumann, boundary condition with scattering in and around the specular direction.

Varying the azimuthal angle of incidence ϕ_0, for a rough, anisotropic surface, Fig. 4.5, $\delta = \lambda$ and $a_1 = 2\lambda$, shows a large variation in the scattering pattern as the incident beam is moved, and a clear difference between the boundary conditions. When the azimuthal angle of incidence is moved from along the minor correlation axis to the major correlation axis, the scattering pattern changes from a mix of forward and backward scattering at $\phi_0 = 0°$. Going to $\phi_0 = 45°$, there is a new peak at $\phi_s = 180° - \phi_0$, similar to what is seen in Ref. [12] for electromagnetic waves. At $\phi_0 = 90°$ the most of the scattered intensity goes into a diffuse peak in the forward scattering direction. The specular peaks and enhanced backscattering is at polar angle of incidence $\theta_s = \theta_0$ for both boundary conditions, not like what is seen for the Dirichlet boundary condition for less rough surfaces, Fig. 4.4, where $\theta_s > \theta_0$

The boundary conditions differ in that there are more pronounced enhanced backscattering for the Dirichlet boundary condition, the peak at $\phi_s = 180° - \phi_0$ is stronger at $\phi_0 = 45°$, and the forward scattering is more diffuse at $\phi_0 = 90°$.

When the azimuthal angle of incidence is kept at $\phi_0 = 45°$ and the anisotropy ratio, r, is changed, Fig. 4.6, going from an isotropic surface to a strongly anisotropic surface, $r \in [1.0, 3.5]$, the scattering pattern goes from purely backscattering to the "bandy stick" shaped region of high intensity seen in Ref. [12] for $r = 1.5$ and $r = 2.0$. Increasing the anisotropy ratio further to $r \geq 2.5$ a high intensity peak in the forward direction and in the $\phi_s = 180° - \phi_0$ direction is seen, both at $\theta_s = \theta_0$. Note the scaling of the in Figs. 4.6(e) and 4.6(f), as the scattering in the forward and $\phi_s = 180° - \phi_0$ direction gets more concentrated as the anisotropy ratio is increased.

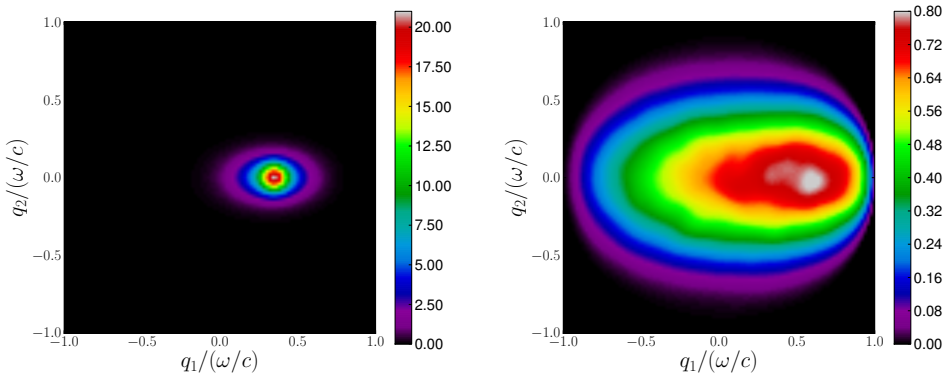

(a) $\phi_0 = 0°$, $\delta = 0.1\lambda$

(b) $\phi_0 = 0°$, $\delta = 0.5\lambda$

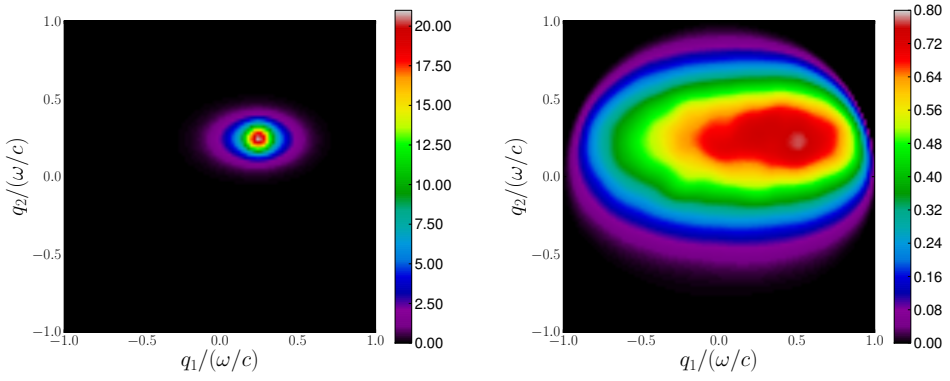

(c) $\phi_0 = 45°$, $\delta = 0.1\lambda$

(d) $\phi_0 = 45°$, $\delta = 0.5\lambda$

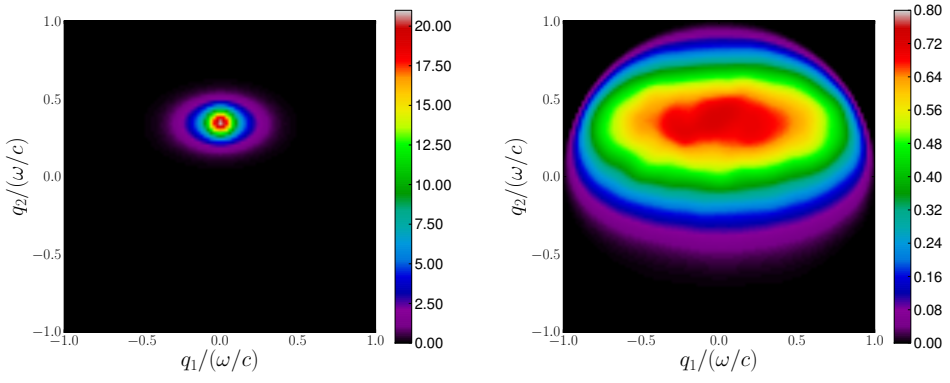

(e) $\phi_0 = 90°$, $\delta = 0.1\lambda$

(f) $\phi_0 = 90°$, $\delta = 0.5\lambda$

Figure 4.4: MDRC scattered from anisotropic surfaces with RMS-roughness $\delta = 0.1\lambda$ and $\delta = 0.5\lambda$, major axis correlation length $a_1 = 2.0\lambda$ and anisotropy ratios $r = 2.0$, for a quadratic surface with length $L = 16\lambda$. The surface is modelled as a Dirichlet boundary condition. The simulations were performed using various azimuthal angles of incidence, ϕ_0. The results were averaged over $N_s = 3500$ samples. The incident beam were a Gaussian beam with half width $w = 4\lambda$ and polar angle of incidence $\theta_0 = 20°$.

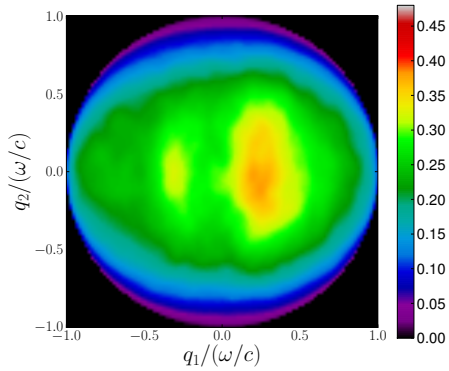

(a) $\phi_0 = 0°$, Neumann BC

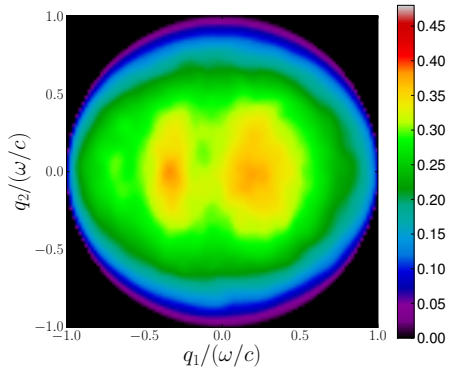

(b) $\phi_0 = 0°$, Dirichlet BC

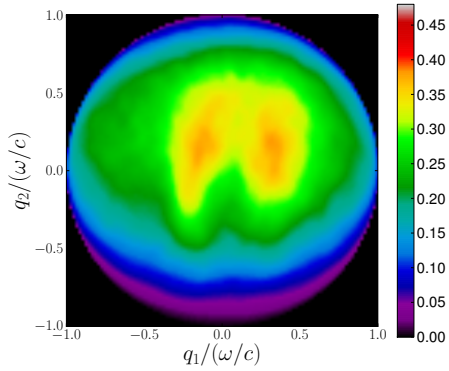

(c) $\phi_0 = 45°$, Neumann BC

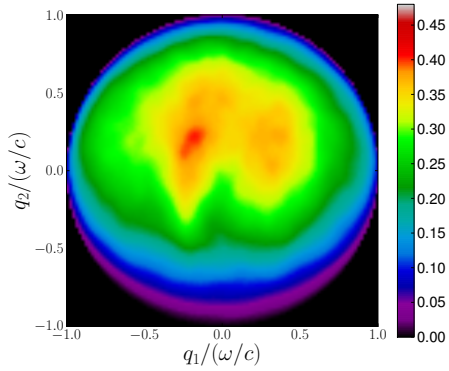

(d) $\phi_0 = 45°$, Dirichlet BC

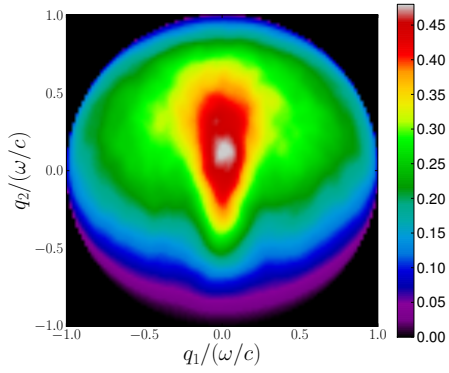

(e) $\phi_0 = 90°$, Neumann BC

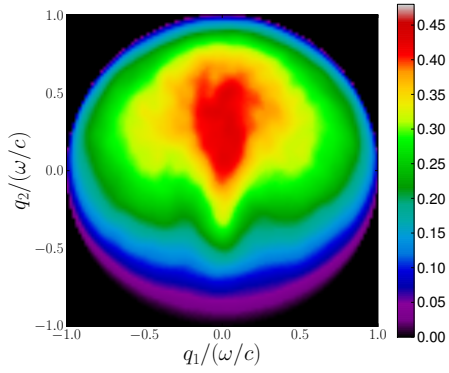

(f) $\phi_0 = 90°$, Dirichlet BC

Figure 4.5: MDRC scattered from an anisotropic surface with RMS-roughness $\delta = 1.0\lambda$, major axis correlation length $a_1 = 2.0\lambda$ and anisotropy ratio $r = 2.0$, for a quadratic surface with length $L = 16\lambda$. The simulations were performed using various azimuthal angles of incidence, ϕ_0, and both Neumann and Dirichlet boundary conditions. The results were averaged over $N_s = 3000$ samples. The incident beam were a Gaussian beam with half width $w = 4\lambda$, polar angle of incidence $\theta_0 = 20°$.

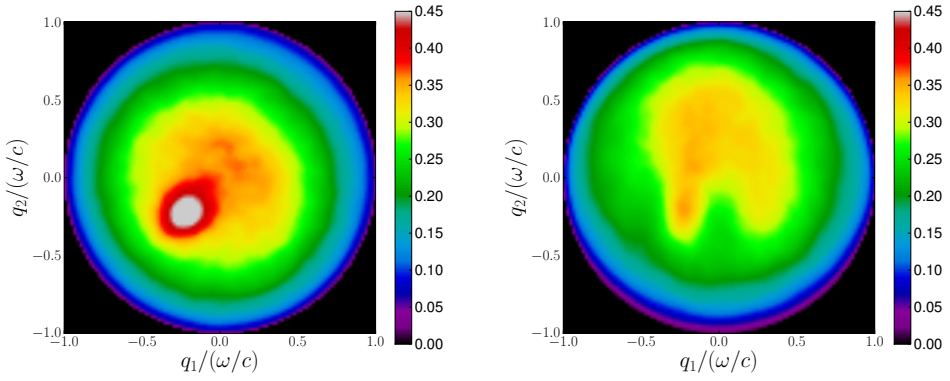

(a) $r = 1.0$

(b) $r = 1.5$

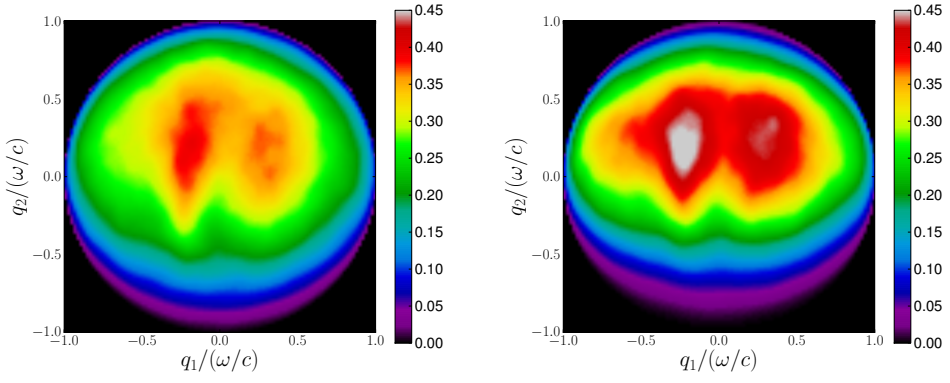

(c) $r = 2.0$

(d) $r = 2.5$

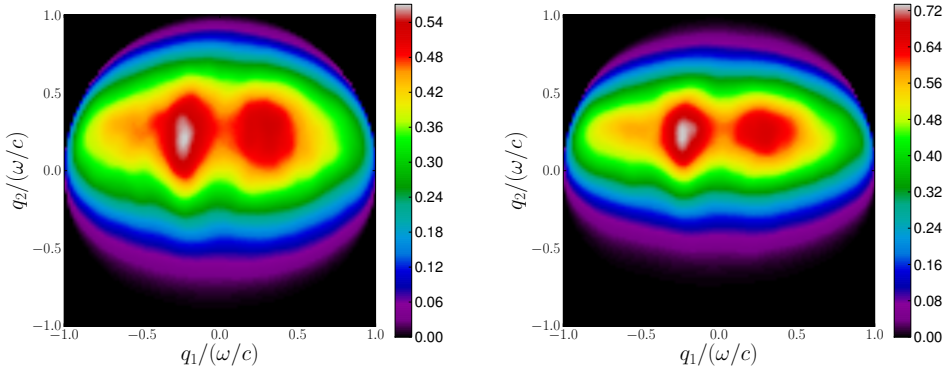

(e) $r = 3.0$

(f) $r = 3.5$

Figure 4.6: MDRC scattered from an anisotropic surface with RMS-roughness $\delta = 1.0\lambda$, major axis correlation length $a_1 = 2.0\lambda$ and various anisotropy ratios for a quadratic surface with length $L = 16\lambda$. The surface is modelled as a Dirichlet boundary condition. The results were averaged over $N_s = 5000$ samples. The incident beam were a Gaussian beam with half width $w = 4\lambda$, polar and azimuthal angle of incidence $\theta_0 = 20°$ and $\phi_0 = 45°$, respectively. Figures (e) and (f) has a different scaling than figures (a)-(d).

4.1.5 Polar angle of incidence

For isotropic surfaces, the rotational invariance gives that the polar angle of incidence is the only relevant parameter describing the incident beam angle. The polar scattering angle is limited to $\theta_0 = 40°$, as the large angle effects discussed in Sec. 3.1 is prominent for incident polar angles larger than $\theta_0 = 40°$.

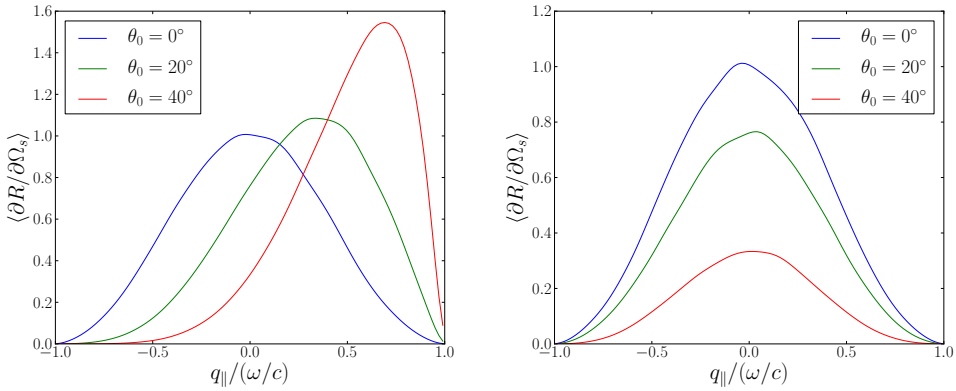

(a) In-plane

(b) Out-of-plane

Figure 4.7: In-plane and out-of-plane scattered intensity for $\theta_0 \in \{0°, 20°, 40°\}$. The surface has a correlation length of $a = 2\lambda$, roughness $\delta = 0.3\lambda$, length $L = 16\lambda$ and no anisotropy. The incident Gaussian wave has a half width $w = 4\lambda$. The surface is described by a Dirichlet boundary condition. The results have been averaged over $N_s = 3000$ samples.

When the polar angle of incidence is increased, Fig. 4.7, the main contribution stays in the specular direction. As seen in the in-plane cuts, the tails change with the distance from the specular peak. The scattered intensity drops off relative to the distance from the specular peak. For larger scattering angles, the peak value is increased as the momentum grid gives smaller grid elements at large scattering angles and shifted to the right in the plot as the grid has smaller grid elements on the high scattering angle side of the peak.

The out-of-plane scattering pattern is as expected, the MDRC is distributed symmetric around the plane of incidence, and the contribution at the centre of the surface is reduced as the forward peak moves towards higher scattering angles. An alternative approach is to study the scattering out of plane at the peak value. This gives the same pattern as the $\theta_0 = 0°$ line, scaled with the increase seen in the in-plane figure.

4.1.6 Coherent and incoherent components

Considering the coherent and the incoherent components separately, we study how the contribution from coherent and incoherent contribution changes with the roughness of the surface.

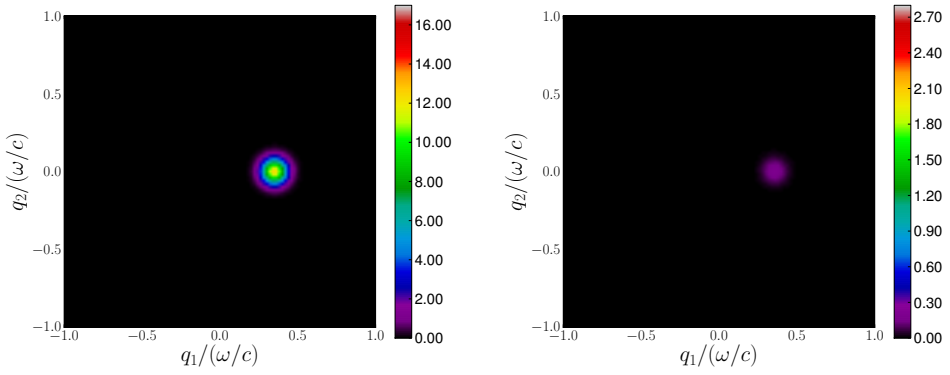

(a) Coherent, $\delta = 0.1\lambda$

(b) Coherent, $\delta = 0.2\lambda$

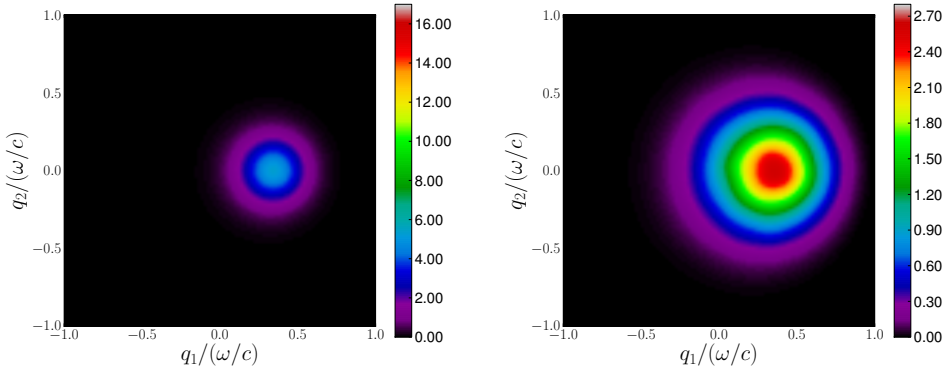

(c) Incoherent, $\delta = 0.1\lambda$

(d) Incoherent, $\delta = 0.2\lambda$

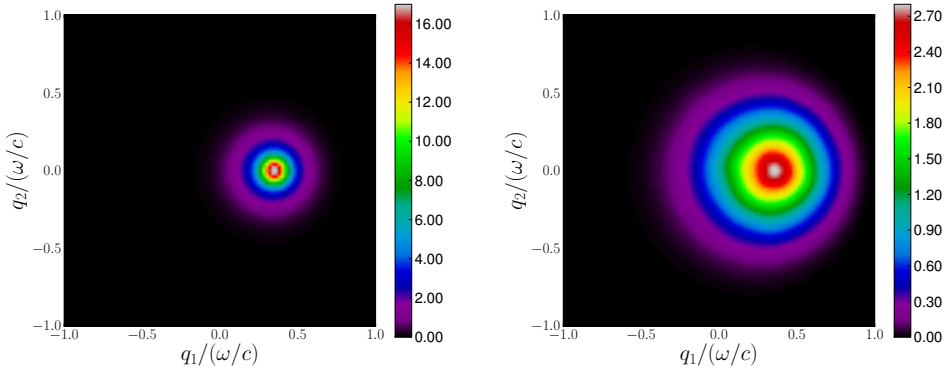

(e) Coherent and incoherent, $\delta = 0.1\lambda$

(f) Coherent and incoherent, $\delta = 0.2\lambda$

Figure 4.8: Coherent, incoherent and combined MDRC for two surface parameters, $\delta = 0.1\lambda$ and $\delta = 0.5\lambda$. Both isotropic, quadratic, $L = 16\lambda$ surfaces have a correlation length $a = 2\lambda$. The surface is described by a Dirichlet boundary condition. The incident beam were a Gaussian beam with half width $w = 4\lambda$, polar and azimuthal angle of incidence $\theta_0 = 20°$ and $\phi_0 = 0°$, respectively. The results have been averaged over $N_s = 3500$ samples.

For less rough surfaces the coherent component of the scattered intensity gives a large contribution in the specular direction, Fig. 4.8. As the surface roughness is increased, the contribution from the coherent component to the mean differential reflection coefficient is reduced. The reflected intensity goes from mainly coherent to mainly incoherent as the surface roughness is increased. For the more rough surfaces, the contribution from coherent scattering will be averaged out, as the coherent scattering depends more on the surface realisation than the underlying process generating the surface.

4.1.7 Comparison with electromagnetic field

Using a perfect electric conductor and a hard wall surface with similar surface statistics, the scalar wave simulation can be compared with electromagnetic (EM) waves (light). We compare the scalar wave scattering with the scattering for a p-polarised incident beam, where the polarisation of the scattered light is not recorded. Comparing the scalar wave and the polarised wave equation is expected to give similar results as long as the contribution from cross-polarised light is low.

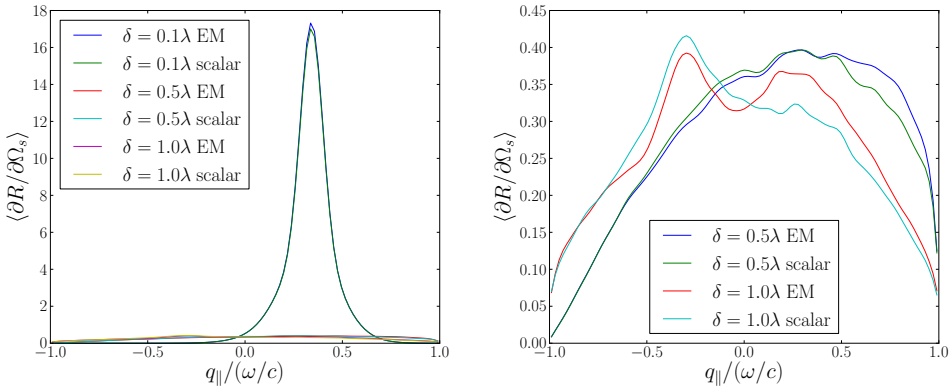

(a) Low δ

(b) High δ

Figure 4.9: In-plane MDRC scattered from a isotropic, Gaussian correlated surface with correlation length $a = 2\lambda$ and length $L = 16\lambda$. We consider the scattering from a p-polarised electromagnetic incident wave (light), and do not record the polarisation of the scattered light, and compare with a scalar wave scattered off a surface The surface roughness is kept in the range $\delta \in [0.1\lambda, 1.0\lambda]$. The surface is described by a Neumann boundary condition for the scalar wave and as a perfect electric conductor boundary condition for the electromagnetic wave. The results have been averaged over $N_s = 3000$ samples.

Comparing the scalar wave and the electromagnetic wave, Fig. (4.9), gives indistinguishable results for a less rough surface, $\delta = 0.1\lambda$, correlation length $a = 2\lambda$. Increasing the surface RMS-roughness to $\delta = 0.5\lambda$, the scalar and EM wave behaves similarly,

but the EM wave has a shift towards larger polar scattering angle θ_s compared to the scalar wave.

At high surface roughness, $\delta = \lambda$, both the scalar wave and the EM wave have a clear enhanced backscattering peak, but enhanced backscattering for the EM wave is weaker. The EM wave has a larger peak in the forward direction compared to the scalar wave, giving the EM wave almost equal contribution in the forward and backward direction. This suggests that enhanced backscattering gives a significant contribution for scalar waves scattered from a Neumann boundary at lower surface roughness than a similar surface where an electromagnetic wave is scattered from a perfect conductor. Due to the finite amount of surfaces that the results have been averaged over and the highly rough surface used in the simulation, requiring a large ensemble of surfaces to obtain good statistics, the difference might just be an artefact from the simulation.

We do not record the polarisation of the scattered light. If the polarisation of the scattered light is split into its p- and s-polarised components, the scattering pattern is split into a co-polarised and a cross-polarised component, where the co-polarised component lies on and around the plane of incidence, whereas the cross-polarised component lies around the plane normal to the plane of incidence, an effect that can not be reproduced using scalar waves.

4.1.8 Energy conservation

Obtaining the full angular distribution makes it possible to check if the total incident energy is conserved, as seen in Sec. 3.6. Checking the unitarity gives an indication of the simulation quality for various surfaces and incident beams.

L	Incident wave	Method	$\mathcal{U}$
16λ	Plane wave	Rigorous	0.981
16λ	Gaussian, $w = 4\lambda$	Rigorous	1.031
128λ	Gaussian, $w = 32\lambda$	Kirchhoff	1.040

Table 4.1: Unitarity for various surface sizes, L, and incident waves scattered from a quadratic, flat surface with various incident beams from normal incidence. The surface is described by a Dirichlet boundary condition, discretised into $\Delta x = \lambda/7$ sized elements.

The unitarity is, Tab. 4.1, below one when the incident wave is a plane wave, as the edge of the surface is illuminated. The plane wave also gives artefacts from the shape of the surface. The unitarity above one for the Gaussian beam is an artefact from the simulation, probably in the calculation of the power of the incident beam. Changing the integration method used in evaluating Eq. (2.66) does not improve this. The above one unitarity is also observed at normal incidence, where evaluation of the Bessel function gives a contribution of 1.

When the surface roughness is increased, the unitarity drops, due to a large contribution from multiple scattering and because scattering along the surface reach the end of the

surface. Similarly, increasing the polar angle of incidence reduces the unitarity, as more of the edges will be illuminated. Increasing the beam half width, w, without increasing the sample size, L, gives a lower unitarity value, as the edges are illuminated.

As mentioned in Sec. 3.6, the incident beam must be limited in width so that the unwanted effects from illuminating the edge of the surface is low. The half width of the beam and the width of the surface is kept at a constant ratio of $L/w = 4$. This choice is a trade-off between memory requirement, as a large surface size requires calculating and storing a larger matrix when solving the integral equation for the field at the surface, and wanting to simulate a physically realisable system. A large surface is also required allow scattering paths that interact with the surface multiple times before they are scattered back. If we had taken into account surface waves, this would require that the surface is large enough to avoid having surface waves that reach the edge of the simulated surface.

Increasing the surface size and using a wider beam requires a finer discretisation of the parallel wave number grid for the scattered waves. The wider beam gives a sharper peak in the scattering direction, and thus a finer momentum grid must be used to give an accurate representation. As most of the CPU time used in obtaining the solution when using the Kirchhoff approximation comes from calculating the MDRC, and the MDRC calculation run time scales with N_q^2, where N_q is number points in the wave number grid in one dimension, a factor of N_q can be saved by calculating the MDRC only in the plane of incidence. However, this takes away the advantage of being able to check the unitarity of the simulation. Thus, unitarity checks have been performed by obtaining the full angular distribution for the given parameters for surface, incident beam and discretisation, and compared with the single cut angular momentum simulations for the same surface, verifying that simulating a cut of the MDRC gives the same result as extracting a cut of the MDRC from the full angular distribution.

4.2 Self-affine surfaces

We now turn to the two-dimensional self-affine surfaces described in Sec. 2.2.2, using the same rigorous simulation for the scattering process as we used for the Gaussian correlated surfaces. We start by comparing the Kirchhoff approximation solution with the analytical expression for a plane wave and the rigorous simulation with the Kirchhoff approximation. Then we study the effect from changing the surface topothesy and Hurst exponent of the surface, and finally we compare the scalar wave scattering with electromagnetic waves scattered from a similar surface.

4.2.1 Comparison of the Kirchhoff approximation and the analytical solution

Using the analytical expression for the MDRC for a plane wave scattering from a self-affine surface[14], Eq. (3.12), we compare the Kirchhoff simulation result with the analytical result. This serves as a way of checking the simulation results obtained when using the Kirchhoff approximation in the rigorous simulation framework, using a wide, Gaussian incident beam.

The analytical result, Fig. 4.10, is calculated using the Kirchhoff approximation and a plane incident wave. In the simulations, the incident beam illuminates a surface of limited size. Using a plane wave illuminates the edge of the surface, giving a scattering pattern that depends on the geometry of the surface, with some of the incident wave not hitting the surface. Instead, we use a wide, Gaussian beam with beam half width $w = 128\lambda$ and a surface of length $L = 512\lambda$. Using a large surface, and thus a wide beam, the Gaussian beam behaves approximately as the plane wave, Eq. (3.1). Limiting the incident wave with a Gaussian envelope makes sure that the incident field is close to zero at the edge of the surface.

The numerical solution gives the same shape and scaling with the topothesy as the analytical solution for all topothesy values $\ell \in [10^{-3}\lambda, 10^{-6}\lambda]$. The numerical solution is consistently above the analytical solution at large scattering angles, and lower than the analytical solution in the specular direction. Some of the difference can be explained by the fact that we are comparing a plane wave and an approximation to a plane wave from a wide, Gaussian wave.

Some difference is expected from the fact that the simulations are based on generated surfaces with a given Hurst exponent and topothesy, averaged over a large number of surfaces, whereas the analytical solution uses the Hurst exponent and topothesy directly. The result shows that the surface generator for self-affine surfaces gives reasonably correct surfaces. It also confirms that the simulation gives reasonable results for wide incident beams and large surfaces.

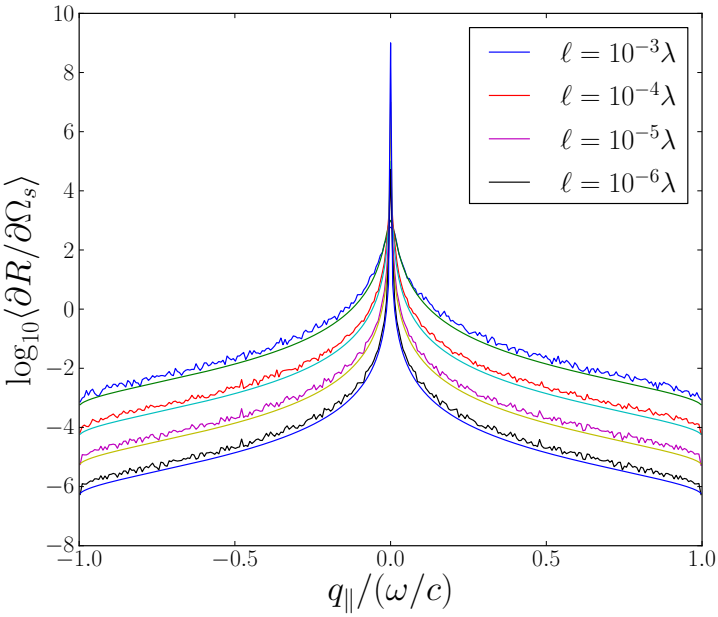

Figure 4.10: Comparison of the MDRC in the plane of incidence from the analytical, plane wave solution and simulation based on the Kirchhoff approximation for a $H = 0.5$ and topothesy $\ell \in [10^{-3}\lambda, 10^{-6}\lambda]$ self-affine surface. The surface is illuminated by a Gaussian beam of half width $w = 128\lambda$ with normal incidence, illuminating a quadratic surface of length $L = 512\lambda$. The surface is described by a Neumann boundary condition. The results have been averaged over $N_s = 1500$ samples.

4.2.2 Comparison of the Kirchhoff approximation and rigorous simulation

For less rough surfaces, where the effect from multiple scattering is limited, simulations using the Kirchhoff approximation and the rigorous simulations is expected to give similar results. As the surface size that can be simulated is limited in the rigorous simulation, both the solution based on the Kirchhoff approximation and rigorous simulation is done on a quadratic, $L = 16\lambda$ sized surface. The Gaussian incident beam has a half width $w = 4\lambda$, to avoid illuminating the surface edges.

The Gaussian shape of the incident beam is seen in the specular direction, Fig. 4.11, for low topothesy. Outside the Gaussian peak, the intensity drops off for larger scattering angles. Compared with the Kirchhoff approximation, the rigorous simulation result drops off faster in the tails. This caused by taking into account multiple scattering, as the multiple scattering paths will be ignored when using the Kirchhoff approximation, whereas the rigorous simulation will retain the multiple scattering. Thus, paths that hits the surface once and is scattered in the downward direction will be ignored in the Kirchhoff approximation, but in the rigorous simulation they will be scattered

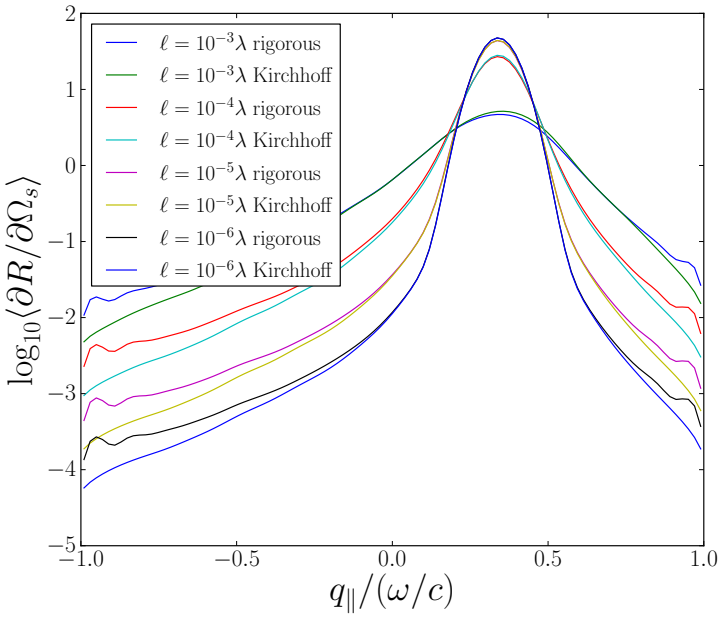

Figure 4.11: Mean differential reflection coefficient for a scalar wave scattered from a self-affine surface with Hurst exponent $H = 0.65$ and varying topothesy. The incident Gaussian wave has a half width $w = 4\lambda$ and hits the surface with a polar angle of incidence $\theta_0 = 20°$. The surface is quadratic and of length $L = 16\lambda$. The surface is described by a Neumann boundary condition. The results have been averaged over $N_s = 2500$ samples.

multiple times, and the multiple scattering paths will have a higher chance of being scattered back at high scattering angles. The bump at very high scattering angles is an artefact from the simulation. As the surface roughness and average slope is increased, the Kirchhoff approximation breaks down, seen as the difference between the rigorous result and the Kirchhoff result is larger for surfaces with high topothesy.

The difference between the rigorous result and Kirchhoff approximation in the specular peak for $\ell = 10^{-3}\lambda$ shows that the Kirchhoff approximation begins to have problem when the surface gets this rough. The Kirchhoff approximation solution gives a peak at higher polar scattering angle than the rigorous simulation. The simulation is performed using the Neumann boundary condition, so the shift is not caused by the behaviour seen in Sec. 2.4.1.

4.2.3 Varying Hurst exponent

The Hurst exponent is kept in the range $0 < H < 1$. When $H = 1/2$ the surface is generated by a random walk. For $H > 1/2$ the profile is correlated and for $H < 1/2$ the profile is anti-correlated. As the Hurst exponent is increased, the surface becomes

calmer.

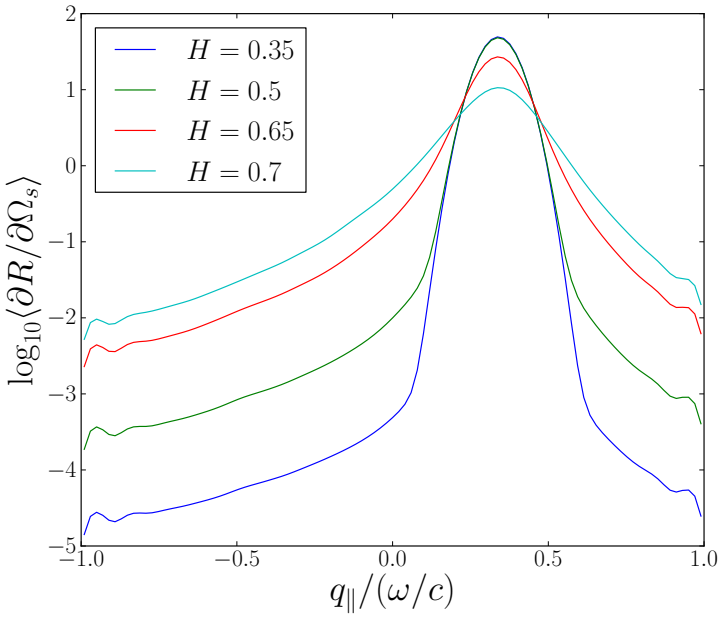

Figure 4.12: The MDRC in the plane of incidence for a scalar wave scattered from a self-affine surface with topothesy held at $\ell = 10^{-4}\lambda$, and Hurst exponent in the range 0.35-0.7. The Gaussian incident beam has a polar angle of incidence $\theta_0 = 20°$ and half width $w = 4\lambda$. The surface is described by a Neumann boundary condition. The results have been averaged over $N_s = 2000$ samples.

As the Hurst exponent is increased, Fig. 4.12, keeping the topothesy constant at $\ell = 10^{-4}\lambda$, the contribution in the forward scattering direction is reduced and the intensity at high scattering angles increases. The Gaussian peak in the forward scattering direction is preserved for low topothesies, but the peak gets wider as the Hurst exponent is increased, and the amount of diffuse scattering is increased.

The transition from the Gaussian peak in the forward direction for $H = 0.35$ is sharp, giving an almost flat background intensity outside the forward peak. At $H = 0.7$, the transition between the forward peak and the diffuse scattering is much smoother, both as the Gaussian peak is wider at the top and the diffuse scattering is stronger.

4.2.4 Varying topothesy

The topothesy of the surface, Eq. (2.12), determines how the surface roughness is scaled over a surface interval, giving a measure of the surface roughness together with the Hurst exponent.

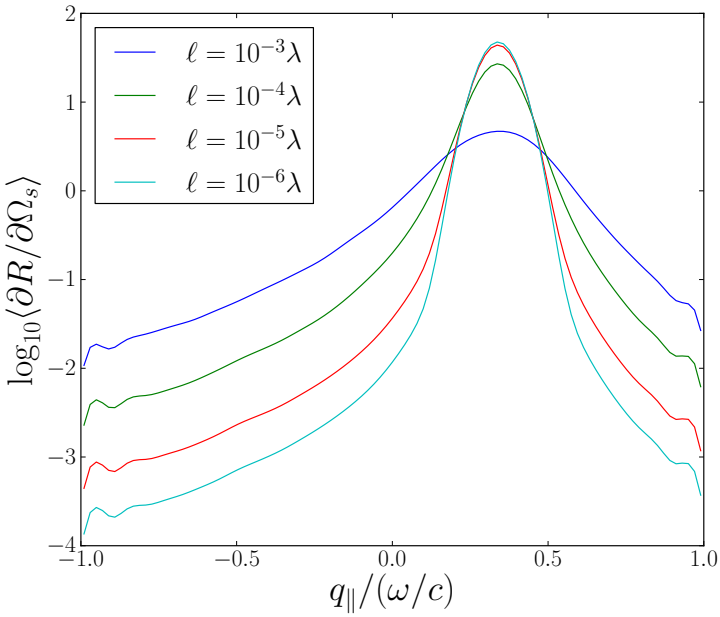

Figure 4.13: The MDRC in the plane of incidence for a scalar wave scattered from a self-affine surface with Hurst exponent held at $H = 0.65$ and topothesy in the range $10^{-3}\lambda - 10^{-6}\lambda$. The Gaussian incident beam has a polar angle of incidence $\theta_0 = 20°$ and half width $w = 4\lambda$. The surface is described by a Neumann boundary condition. The results have been averaged over $N_s = 2500$ samples.

As the topothesy is increased, Fig. 4.13, the contribution in the specular direction is reduced and is smoothed out into a wider peak with higher intensity at high scattering angles. Keeping the Hurst exponent at $H = 0.65$ and going from $\ell = 10^{-6}\lambda$ to $\ell = 10^{-5}\lambda$ changes little in the forward scattering direction, but gives a large increase at large scattering angles. When the topothesy is increased further to $\ell = 10^{-4}\lambda$ and $\ell = 10^{-3}\lambda$, the forward peak widens further and the large scattering angle intensity grows larger. When the topothesy is increased, we see a similar to what is observed when the Hurst exponent is increased, but the shape of the forward peak is not changed in the same way, but rather makes a smooth translation from a smooth peak to a wide peak.

For a plane wave scattered from a self-affine surface, one can find the peak value and half-width at half-maximum as a function of surface topothesy [11]. This method is less applicable for our Gaussian incident beam, as the scattered intensity depends more on the shape of the incident beam than on the surface for less rough surfaces. Even for the wide, Gaussian beam used in Sec. 4.2.1, the incident beam shape is seen in the scattered beam, giving almost the same peak value for the $\ell = 10^{-5}\lambda$ and the $\ell = 10^{-6}\lambda$ surface.

The topothesy determines how much of the incident power will be scattered away from

the specular direction, compared to the amount of specular scattering, but the shape of the forward scattering peak and the shape of the intensity pattern outside the specular peak changes less than when the Hurst exponent is changed.

4.2.5 Constant slope

The average slope over a short distance, as defined in Eq. (2.21), gives a coupling between the effect from changing the Hurst exponent and the topothesy. The average slope is kept constant over a range of Hurst exponents, changing the topothesy accordingly. The slope largely determines how the system behaves as long as the Kirchhoff approximation is valid, as the scattering then only is dependent on local slope and the Fresnel coefficients.

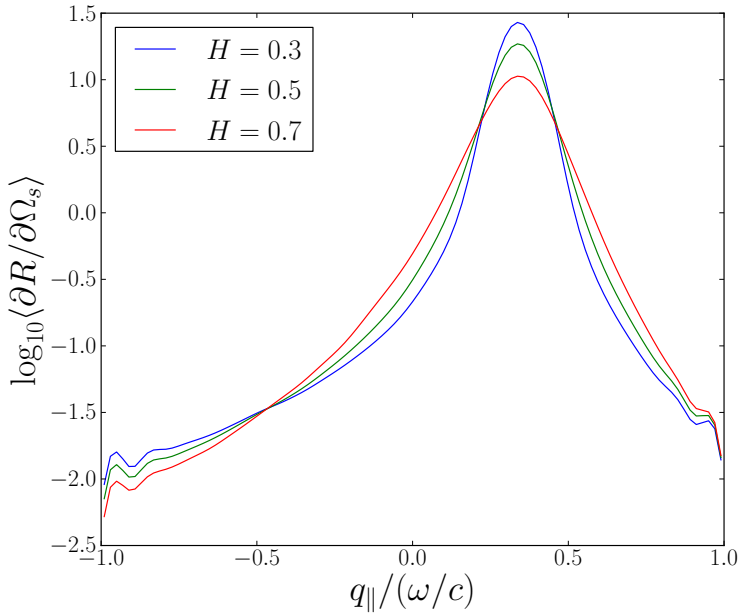

Figure 4.14: In-plane MDRC for scattering from a self-affine, quadratic surface of length $L = 16\lambda$ with constant slope, $s = 0.0631\lambda$, for three Hurst exponents: $H = 0.3$, $\ell = 1.93 \cdot 10^{-2}\lambda$, $H = 0.5$, $\ell = 3.98 \cdot 10^{-3}\lambda$ and $H = 0.7$, $\ell = 10^{-4}\lambda$. The surface is described by a Neumann boundary condition. The Gaussian incident beam has a polar angle of incidence $\theta_0 = 20°$ and half width $w = 4\lambda$. The results have been averaged over $N_s = 5000$ samples.

The resulting scattering pattern in the plane of incidence, Fig. 4.14, changes little as the Hurst exponent changes when the slope is held constant. However, the peak in the specular direction gets wider as the Hurst exponent is increased, giving a less steep fall off close to the specular peak and steeper fall off at large scattering angles, compared

to the low Hurst exponent scattering pattern with the same slope. The peak value is reduced for high Hurst exponents.

As the scattering pattern still depends on the Hurst exponent, there is more than just the mean slope affecting the scattering pattern. For a given Hurst exponent, the mean slope is just a rescaled measure of the surface topothesy.

4.2.6 Hurst exponent and topothesy outside the validity of the analytical expression

The analytical solution, based on the Kirchhoff approximation, breaks down as the roughness of the surface grows large. Using the rigorous simulation approach, the surface roughness can be larger than what can be solved with the Kirchhoff approximation. The Kirchhoff approximation gives reasonable results as long as the surface varies slowly at the wavelength length scale and the contribution from multiple scattering can be neglected. As the surface roughness is increased, the contribution from multiple scattering is seen in the rigorous simulation, first at large scattering angles.

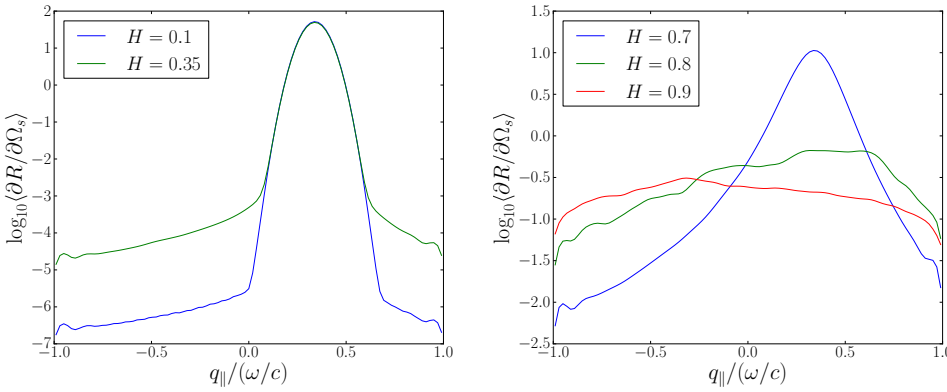

(a) Low H (b) High H

Figure 4.15: MDRC for a scalar wave scattered from surfaces with low and high Hurst exponent, keeping the topothesy at $\ell = 10^{-4}\lambda$. The surface is described by a Neumann boundary condition. The Gaussian incident beam has a half width $w = 4\lambda$ and hits the surface with polar angle $\theta_0 = 20°$. The results have been averaged over $N_s = 2000$ samples.

Reducing the Hurst exponent further below what was done in Sec. 4.2.4, Fig. 4.15(a), $H < 0.35$, only gives a clearer peak in the specular direction and less scattering outside the specular direction, when the topothesy is held unchanged at $\ell = 10^{-4}\lambda$. For Hurst exponents in this range, the anti-correlated surface function will fluctuate fast compared to the wavelength, giving a surface that is approximately flat at the wavelength length scale.

When the Hurst exponent is increased above $H = 0.7$, Fig. 4.15(b), the correlated

surface has so large peaks, in spite of the low local fluctuations, that the simulation breaks down, giving results that no longer describes the physics of the system. For even more rough surfaces, $H > 0.9$, the system matrix solver in the simulation no longer converge. However, some insights can be extracted from the results. At $H = 0.8$, the forward peak is approximately in the specular direction, but with a lot of diffuse scattering. When the Hurst exponent is increased further to $H = 0.9$, the scattering pattern is almost flat, but with a small peak in the backscattering direction. This might be caused by enhanced backscattering, but might also just be an artefact in the simulation.

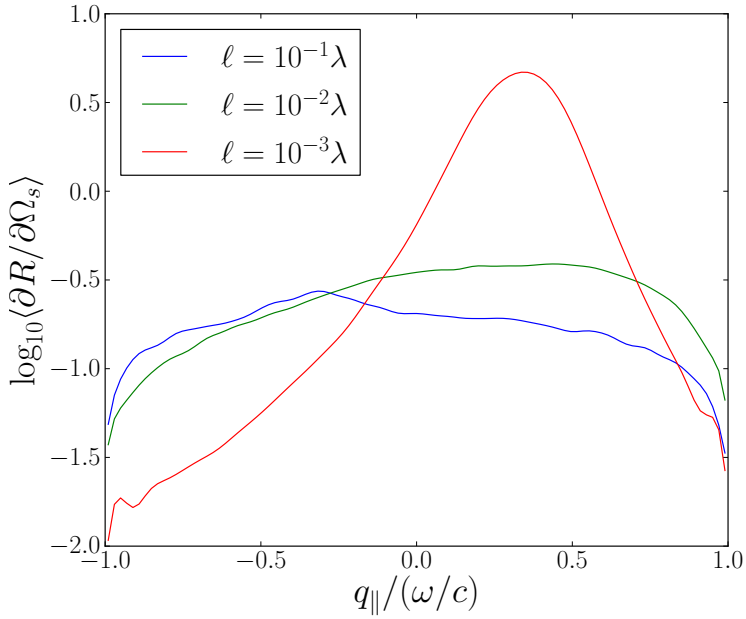

Figure 4.16: In-plane MDRC for a scalar wave scattered from surfaces with high topothesy, keeping the Hurst exponent at $H = 0.65$. The surface is described by a Neumann boundary condition. The Gaussian incident beam has a half width $w = 4\lambda$ and hits the surface with a polar angle $\theta_0 = 20°$. The results have been averaged over $N_s = 1500$ samples.

As the topothesy is increased, Fig. 4.16, the specular scattering is reduced and incoherent scattering outside the specular direction is increased. Increasing the topothesy further gives surfaces with large local variations, such that the simulations give unreliable results. As for the high Hurst exponent result, the scattering pattern reduces to a wide, even distribution in all directions with a small peak in the forward direction, and when the topothesy is increased even further, there is a small peak in the backward direction. When the topothesy is increased above $\ell = 10^{-1}\lambda$, the simulation no longer converges.

4.2.7 Self-affine surfaces and electromagnetic waves

As for the surface with a Gaussian correlation function, the waves scattered from a self-affine surface behaves similarly for a scalar wave and for an electromagnetic wave (light) when the polarisation of the scattered light is ignored.

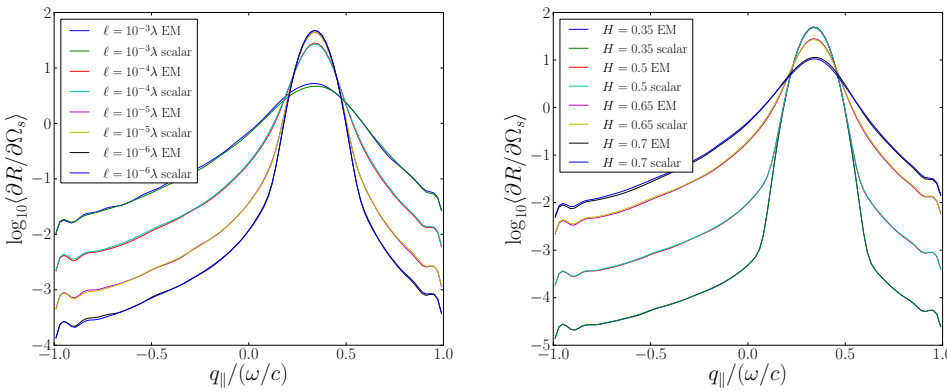

(a) Varying topothesy

(b) Varying Hurst exponent

Figure 4.17: In-plane MDRC for a electromagnetic wave (light) scattered from a self-affine surface, compared to a scalar wave with similar surface parameters, using a Gaussian p-polarised incident beam with half width $w = 4\lambda$. The surface is described by (a) $H = 0.65$, $\ell \in \{10^{-3}\lambda, 10^{-4}\lambda, 10^{-5}\lambda, 10^{-6}\lambda\}$ (b) $\ell = 10^{-4}\lambda$, $H \in \{0.35, 0.5, 0.65, 0.7\}$. The polarisation of scattered intensity of the EM wave is not recorded. The surface is described by a Neumann boundary condition for the scalar wave scattering and perfect electric conductor boundary condition for the electromagnetic scattering. The results have been averaged over $N_s = 3000$ samples.

For the self-affine surfaces, the scalar and the electromagnetic wave, Fig. 4.17, behaves similarly. A minor difference is seen in the scattered pattern for the more rough surfaces, the $H = 0.7$, $\ell = 10^{-4}\lambda$ and the $H = 0.65$, $\ell = 10^{-3}\lambda$ surface, where the EM wave lies higher than the scalar wave in the forward peak, and lower at large scattering angles. This resembles the effect seen for the Gaussian correlated surfaces in Sec. 4.1.7, but less pronounced. For less rough surfaces where the scattering is largely directed in the specular direction, the scalar scattering and the electromagnetic scattering behaves similarly. For two-dimensional surfaces, cross polarisation of scattered light will have an impact on how the scattering pattern behaves, but this effect is limited for less rough surfaces.

4.3 Parallelisation

The trivially parallelisable matrix generation and MDRC calculation were parallelised using OpenMP. The timing results were performed on a 4-core Intel Core i7-920 running at 2.67GHz. Parallelisation of the matrix generation and MDRC calculation, Tab. 4.2,

Parallelised component	1 CPU (s)	4 CPUs (s)
Rigorous		
matrix generation	482 (1.00)	378 (1.28)
MDRC calculation	482 (1.00)	269 (1.79)
matrix gen. and MDRC calc.	482 (1.00)	182 (2.65)
Kirchhoff		
MDRC calculation	266 (1.00)	68 (3.90)

Table 4.2: Timing (and speed-up) for the various methods, using 1 and 4 CPUs. The MDRC is averaged over $N_s = 10$ samples for scattering from a quadratic, Gaussian correlated isotropic, quadratic, $L = 16\lambda$ surface with correlation length $a = 2\lambda$ and RMS-roughness $\delta = 0.1\lambda$, illuminated by a Gaussian beam from three different angles of incidence. The iterative solver converged after about 10 iterations. The code is parallelised using OpenMP with the Intel Fortran compiler, ifort.

gives a speed up of 2.65 running on 4 CPUs. Parallel calculation of the scattered field from the surface field makes a significant difference, but gives a far from linear speed-up in the rigorous simulation, as the CPU-time spent calculating the physical observables is low compared to the time used to calculate the system matrix elements and solving the matrix system. However, when using the Kirchhoff approximation, the calculation of physical observables is the heaviest part of the calculation, giving a speed up of 3.90 on 4 CPUs. The speed-up depends on the amount of calculation that is done serially. The results in Tab. 4.2 were performed on a less rough surface where the serial iterative solver converged after about 10 iterations. For a more rough surface, more time will be spent in the matrix solver, and thus the speed-up will be lower.

The OpenMP implementation in the Portland Group Fortran 95 compiler, pgf95, has some problems with reporting CPU usage. The resource usage reported is inconsistent after the first parallel loop, and also suffered from seemingly random segmentation faults. The problem still persists in a minimal example using OpenMP, and the PG documentation and support were less helpful. As a workaround for this, the necessary modifications were done on the code, build system and libraries to support the Intel Fortran 95 compiler, ifort. All simulations with parallel code were done using ifort.

4.4 Further work

The simulation approach presented here is limited to simple surface models, simple media, static surfaces and only isotropic self-affine surfaces. Further work might include:

4.4.1 Other surface models

The hard wall approximation for acoustic waves corresponds in many respects to the perfect conductor for EM waves, where there are no propagation through the lower media. In a real surface, the surface will not behave perfectly as a hard wall. If the lower media allows for propagating waves, there will be transmission through the lower media. A more realistic scattering model allows for lateral and transverse surface waves in the lower media, corresponding to surface plasmon polarisations in the EM model.

4.4.2 Time varying surface

Scattering from moving surfaces, where the statistical properties stays unchanged as the surface changes. The sea surface, affected by wind and current, is one example of such a surface.

4.4.3 Scattering from anisotropic self-affine surfaces

As the anisotropic correlated surface, the self-affine surface can have different parameters in different directions in the surface. If the Hurst exponent is different along the minor an major axis, the scattering pattern will depend on the incident azimuthal angle, and the scattered intensity will no longer be symmetric around the plane of incidence. This can be studied further using the same techniques as in Ref. [12].

4.4.4 Using a more realistic acoustic model

The approximate solutions used in Refs. [20, 4] allows us to use more realistic propagation models and accounting for transmission loss. This can be extended to scattering in non-homogeneous media with a non-homogeneous velocity profile and combined scattering and reflection in layered media.

5 Conclusion

We have a working implementation of scalar waves scattered from a randomly rough surface using hard wall and free surface boundary conditions. The approach takes into account multiple scattering in the surface roughness. The resulting simulations give a detailed view of how the surface parameters influence the scattering pattern. The results have been compared to the analytical expression for a plane wave scattered from a self-affine surface, giving a good indication that the simulation approach and the surface generator give reasonable results. We have also compared the results to polarised, electromagnetic waves (light), where the scalar wave scattering from a hard wall surface gives results comparable to EM waves scattered from a perfect conductor when the polarisation of the scattered light is not recorded. We observe several of the expected phenomena in the scattering pattern, such as specular scattering for less rough surfaces, diffuse forward scattering as the surface roughness increased and enhanced backscattering for systems dominated by second order multiple scattering. The results from using hard wall and free surface boundary conditions is the same for less rough surfaces, as the scattered intensity for both boundary conditions is equal in the Kirchhoff approximation, but as the surface roughness increases, the scattering pattern depends on the boundary conditions. When the surface roughness is increased further so that multiple scattering gives a large contribution, the difference between the two boundary condition again diminishes.

Using a correlated surface with a Gaussian correlation function, the scattering pattern depends on the surface RMS-roughness and the correlation length. When an anisotropy is introduced in the correlation function, much of the same behaviour seen with polarized waves is observed. The in-plane and out-of-plane cuts no longer gives a good view of the scattering pattern, as the symmetry, with respect to the plane of incidence, observed for isotropic surfaces is no longer valid, with some of the scattering peaks peaks moving away from the plane of incidence. For self-affine surfaces, the scattering pattern changes with the topothesy and the Hurst exponent of the surface. Highly correlated surfaces with $H > 0.7$ makes the calculation difficult, as the surface has large peaks and dips, but with little small scale fluctuations. Similarly, as the topothesy is increased above $\ell = 10^{-3}\lambda$, the large roughness of the surface makes the calculation difficult. Coupling the Hurst exponent and the topothesy into a measure for the mean slope gives a single parameter for the surface roughness, valid for less rough surfaces. However, the scattered intensity in the forward direction still becomes wider as the Hurst exponent increases.

Our approach is limited to plane, ergodic surfaces, where the simulation can be averaged over a large number of small surface realisations. The scattering model is limited to hard wall and free surface boundary conditions, not supporting propagating waves in the lower media or surface waves.

Bibliography

[1] M. Abramowitz and I. A. Stegun. *Handbook of Mathematical Functions with Formulas, Graphs, and Mathematical Tables*. Dover, New York, NY, USA, 9th edition, 1964.

[2] National Science Foundation and Department of Energy. BLAS. http://www.netlib.org/blas/, 2010.

[3] J.D. Jackson. *Classical electrodynamics*. John Wiley & Sons, Inc., New York, NY, USA, 3rd edition, 1998.

[4] F. B. Jensen, W. A. Kuperman, M. B. Porter, and H. Schmidt. *Computational ocean acoustics*. Springer-Verlag, New York, NY, USA, 2000.

[5] A. Mendoza-Suárez and E. R. Méndez. Light scattering by a reentrant fractal surface. *Appl. Opt.*, 36(15):3521–3531, May 1997.

[6] A. Mendoza-Suárez and E. R. Méndez. Derivation of an impedance boundary condition for one-dimensional, curved, reentrant surfaces. *Optics Communications*, 134(1-6):241 – 250, 1997.

[7] R. Piessens, E. Dedoncker Kapenga, C. Uberhuber, and D. Kahaner. Quadpack: A subroutine package for automatic integration. 1983.

[8] W. H. Press, S. A. Teukolsky, W. T. Vetterling, and B. P. Flannery. *Numerical Recipes, The Art of Scientific Computing*. Cambridge University, Cambridge, UK, 3rd edition, 2003.

[9] I. Simonsen. Optics of surface disordered systems. *Eur. Phys. J. Special Topics*, 181:1–103, 2010.

[10] I. Simonsen, A. A. Maradudin, and T. A. Leskova. Scattering of electromagnetic waves from two-dimensional randomly rough perfectly conducting surfaces: The full angular intensity distribution. *Phys. Rev. A*, 81(1):013806, Jan 2010.

[11] I. Simonsen, D. Vandembroucq, and S. Roux. Electromagnetic wave scattering from conducting self-affine surfaces: an analytic and numerical study. *J. Opt. Soc. Am. A*, 18(5):1101–1111, May 2001.

[12] Ingve Simonsen, Jacob B. Kryvi, Alexei A. Maradudin, and Tamara A. Leskova. Light scattering from anisotropic, randomly rough, perfectly conducting surfaces. *Computer Physics Communications*, 182(9):1904 – 1908, 2011. Computer Physics Communications Special Edition for Conference on Computational Physics Trondheim, Norway, June 23-26, 2010.

[13] G. L. G. Sleijpen and D. R. Fokkema. BiCGstab(ℓ) for linear equations involving unsymmetric matrices with complex spectrum. *Electron. Trans. Numer. Anal.*, 1(Sept.):11–32 (electronic only), 1993.

[14] D. Strand. Wave scattering from two-dimensional self-affine surfaces. Master's thesis, Norwegian University of Science and Technology, 2011.

[15] V. Strassen. Gaussian elimination is not optimal. *Numerische Mathematik*, 14(3):354–356, 1969.

[16] E. I. Thorsos. The validity of the Kirchhoff approximation for rough surface scattering using a Gaussian roughness spectrum. *J. Acoust. Soc. Am.*, 83(1):78–92, 1988.

[17] P. Tran and A. A. Maradudin. Scattering of a scalar beam from a two-dimensional randomly rough hard wall: Enhanced backscattering. *Phys. Rev. B*, 45:3936–3939, February 1992.

[18] P. Tran and A. A. Maradudin. Scattering of a scalar beam from a two-dimensional randomly rough hard wall: Dirichlet and Neumann boundary conditions. *Appl. Opt.*, 32(15):2848–2851, May 1993.

[19] H. A. van der Vorst. Bi-CGstab: A fast and smoothly converging variant of Bi-CG for the solution of nonsymmetric linear systems. *SIAM J. Sci. Statist. Comput.*, 13(2):631–644, 1992.

[20] A. G. Voronovich. *Wave Scattering from Rough Surfaces*. Springer-Verlag, Berlin, Germany, 2nd edition, 1999.